Journal of Geochemical Exploration 197 (2019) 93–113

Contents lists available at ScienceDirect

Journal of Geochemical Exploration

journal homepage: www.elsevier.com/locate/gexplo

The relative distribution of critical (Sc, REE) and transition metals (Ni, Co, Cr, Mn, V) in some Ni-laterite deposits of New Caledonia

Marc Ulrich[a,*], Michel Cathelineau[b], Manuel Muñoz[c], Marie-Christine Boiron[b], Yoram Teitler[b], Anne Marie Karpoff[a]

[a] IPGS-EOST, CNRS UMR 7516, 1 rue Blessig, 67084 Strasbourg Cedex, France
[b] Université de Lorraine, CREGU, CNRS UMR 7539, GeoRessources, BP 70239, 54506 Vandœuvre-lès-Nancy, France
[c] Géosciences Montpellier, CNRS UMR 5243, 1 place Eugène Bataillon, 34090 Montpellier, France

ARTICLE INFO

Keywords:
Ni-laterites
Scandium
REE
Transition metals
New Caledonia ophiolite

ABSTRACT

The European Union recently updated the list of raw materials considered as critical for its industry on the basis of their high economic importance and their relative supply risk. This list now defines 26 critical raw materials that include among others, rare earth elements (REE), scandium, vanadium and cobalt. Among the different primary resources of these critical metals, lateritic deposits are particularly targeted. Recent investigations have shown that the latter elements can be accumulated during weathering in consequence of residual and secondary enrichment. These environments are also characterized by significant concentrations of transition metals (e.g. Mn, Cr, Ni), which are not defined as critical to date but remain of primary economic importance.

In this study, we investigate the potential enrichment of some critical (REE, Sc, V, Co) and base transition metals (Mn, Cr, Ni) in Ni-lateritic deposits of New Caledonia by combining mineralogical, bulk-rock, and in situ mineralogical and geochemical approaches. In addition, particular attention was paid to the development of a new standard compound, labelled StdGoe 1.1, to ensure accurate and reproducible analyzes of iron oxides by LA-ICP-MS. Based on this new specifically developed standard, the concentrations obtained for most elements present in iron oxides were shown to be significantly lower, by 20 to 50%, compared to concentrations obtained from calibration using the NIST SRM 610 standard. Such discrepancy is attributed to strong matrix contrasts between finely divided iron oxides particules and the silicate glass NIST standard, and highlight that previous concentrations measured by LA-ICP-MS in iron oxides and available to date in the literature must be considered with care.

Based on this new development, our results show that critical and transition metals are concentrated in different horizons of the lateritic profile. Ni mainly concentrates in secondary Ni-bearing phyllosilicates in saproliths, while it is mainly hosted by goethite in limonite levels. Mn and Co both precipitate as Mn-oxides at the interface between saproliths and limonite facies, while they are sorbed into iron oxides (goethite and hematite) after dissolution of Mn-oxides in the upper levels of the profile. The main fraction of Cr and V is hosted by primary chromites, which are weathering-resistant relative to the other minerals. On the other hand, the Cr and V fraction released after pyroxene dissolution is integrated into goethite. Both elements are thus continuously enriched with increasing weathering level. Rare earth elements mainly accumulate in Mn-oxides horizons. Only Ce is concentrated in the uppermost levels of the lateritic profile, likely in the form of cerianite. Sc is mainly hosted by pyroxenes in the bedrock, and shows a progressive enrichment strongly controlled by goethite in the other horizons. Highest concentrations of Sc are observed at the transition between yellow and red laterites, where the highest proportions of goethite are observed. The decrease of Sc concentration in the iron crust horizon, at the top of the laterite profile, is attributed to the progressive dissolution of goethite and subsequent hematite crystallization.

If the very low REE content of New Caledonia laterites reported in this study make them hardly valuable, Sc concentrations are high enough to be potentially exploited as a Ni-Co by-product. Therefore, it could be worth considering Sc as a new potential resource in New Caledonia laterites in the forthcoming decades.

* Corresponding author.
E-mail address: mulrich@unitra.fr (M. Ulrich).

https://doi.org/10.1016/j.gexplo.2018.11.017
Received 18 April 2018; Received in revised form 6 November 2018; Accepted 26 November 2018
Available online 29 November 2018
0375-6742/ © 2018 Published by Elsevier B.V.

1. Introduction

In June 2011, the European Commission emitted a first report entitled Critical Raw Materials for the EU (European Commission, 2011). This report identified a list of 14 raw materials which were defined critical on the basis of their high economic importance and their potential risk of supply. Among these raw materials, most of them are of a primary importance for modern technology, renewable energy and industry (hybrid and electric car industry, wind turbine technology; aerospace industry, portable electronics and so on…). An updated report was published three years later in which 6 raw materials were added to the previous list (European Commission, 2014), and finally last year, a new version assessed a revised list of 26 critical raw materials and groups of raw materials (European Commission, 2017). In this list, rare earth elements (REE) are particularly targeted since China, which produces about 95% of the REE worldwide and is the main EU supplier, has announced a restriction of their exportation to secure their own domestic use. In addition, transition metals like scandium and vanadium, which were not on the 2014 list, are now considered as critical due to an increasing demand in the market (Emsley, 2014; Gambogi, 2018; Polyak, 2018).

Among the different possible sources of critical metals, weathering horizons are particularly investigated. In such environments, REE and other rare metals show limited mobility and thus may be locally enriched through successive processes of leaching and concentration in neoformed silicates, oxides or phosphates (Aiglsperger et al., 2016; Castor and Hendrick, 2006; Chakhmouradian and Wall, 2012; Eliopoulos and Economou-Eliopoulos, 2000). As a consequence, several investigations of the potential occurrence of critical metals (including REE and Sc) have been done recently in Ni-Co laterite deposits developed on ultrabasic basements worldwide, e.g. Cuba, Dominican Republic (Aiglsperger et al., 2016; Villanova-de-Benavent et al., 2014), Indonesia (Maulana et al., 2016), Australia (Chassé et al., 2017; Jaireth et al., 2014), New Caledonia (Audet, 2009). The New Caledonia ophiolite is of major economic importance since it hosts 10% of the world Ni reserves (McRae, 2018). The country is the third main producer of nickel and is also one of the main producers of cobalt (~3% of the world production and reserves; Shedd, 2018). Recent investigations of Sc contents in New Caledonia laterites have shown that significant concentrations occur mainly at the top of the lateritic profile (up to 80 ppm Sc; Audet, 2009). Although these preliminary data show a clear relation between Sc and Fe enrichments, suggesting that Sc is residually enriched at least during the first steps of weathering, little is known about the variation of concentrations in the parent rocks, the concentration factors, and Sc-bearing mineral phases along the weathering.

This study aims at presenting a complete overview of the distribution and concentration of various critical elements (including REE, Sc, Co and V) along the weathering profile of the New Caledonia ophiolite and their relation with the mineralogy. In addition, other transition metals such as Mn, Cr and Ni, not considered as critical but still remaining of major economic importance for EU (European Commission, 2017), are also studied.

2. Geological settings

New Caledonia lies 2000 km east of Australia and corresponds to an emerged part of the Norfolk Ridge micro-continent (Fig. 1). The island consists of a patchwork of two sets of terranes: (i) an Upper Carboniferous to Lower Cretaceous assemblage of metamorphic and volcano-sedimentary terranes, which are related to the formation of an accretionary complex formed during the Jurassic period along the East-Gondwana active margin (Cluzel and Meffre, 2002). These terranes form the present-day autochtonous basement of the island; and (ii) a Campanian to Paleocene allochthonous assemblage of terranes of which origin is related to the opening and subsequent closure of the South Loyalty Basin (e.g. Cluzel et al., 2001; Cluzel et al., 2012; Ulrich et al., 2010; Whattam et al., 2008). Among these terranes, the New Caledonia ophiolite, so-called the Peridotite nappe, is most prominent since it covers about one-third of the island. It consists of a main unit located on the south of the island (i.e. the “Massif du Sud”) and a number of isolated tectonic klippes spread along the West coast (Fig. 1). The ophiolite is dominantly composed by upper mantle rocks (harzburgite and rare lherzolite) with widespread ultramafic (pyroxenite, wherlite, dunite) and mafic (gabbro) cumulates (Allègre and Prinzhofer, 1985; Marchesi et al., 2009; Pirard et al., 2013; Prinzhofer et al., 1980; Secchiari et al., 2016; Ulrich et al., 2010).

Due to the tropical climate at these latitudes, the ophiolite has undergone a strong weathering that probably started during or soon after obduction (Oligocene times, c. 25 ± 5 Ma; Sevin et al., 2012). This weathering has led to the development of a thick lateritic regolith (Fig. 2) that typically comprises five horizons which are in ascending order (i) saprock, (ii) saprolite, (iii) yellow laterite, (iv) red laterite and (v) ferricrete. In saprolite, the primary silicates (olivine/serpentine and pyroxene) are progressively dissolved, resulting in the formation of iron oxyhydroxides, quartz and series of various Mg(Ni) phyllosilicates (serpentine, kerolite, pimelite; Cathelineau et al., 2015b, 2016; Manceau and Calas, 1985). Laterite and ferricrete are dominated by iron oxides (goethite and hematite; Fig. 3) while silicates, are almost completely dissolved (e.g. Trescases, 1973, 1997).

In 2017, Ni-deposits of New Caledonia represented 10% of the nickel production (210 ktons·yr^{-1}) and ~9% of the world reserves (McRae, 2018). Ni-ore is mainly recovered from the saprolite horizons (~4.5 wt% NiO), where Ni accumulates into secondary serpentines (up to 3 wt% NiO) and kerolite (talc-like, up to 30 wt% NiO; Cathelineau et al., 2016; Dublet et al., 2012; Manceau and Calas, 1985). Nickel is the only transition metal to be exploited so far in New Caledonia. The only exception is in the southernmost mining company, namely Goro Nickel (Vale) where Ni-ore occurs in oxide deposits dominated by iron oxyhydroxides such as goethite, with an average Ni grade of 1.6% (e.g. Wells et al., 2009) and where Co is a co-product mainly hosted by Mn hydrous oxides (Manceau et al., 1987, 1992).

3. ANALYTICAL methods

3.1. Sampling strategy

In this study, 65 samples were collected from the Koniambo massif and the Bien Sûr mine, near the Pirogues river in the Massif du Sud (Fig. 1, Table 2). Part of these samples have been collected in four drilled cores (CT, Mia OPB4, Mia OPB7, U0240) and five vertical profiles picked-up on field outcrops. Among these profiles, five are focalized on the uppermost parts of the regolith (i.e. laterite horizons and pisoliths/ferricrete). Others samples correspond to isolated saprolite, laterite or pisolith samples collected randomly in the different horizons of the weathering profile. In addition, two lherzolites and ~15 pisoliths (Fig. 3) have been used to determine the chemical composition of main primary minerals and iron oxides, respectively (Tables 2 and 3).

3.2. X-ray diffraction

Analyses were performed at ISTerre (Grenoble, France) on sample powders. X-ray diffraction (XRD) patterns were recorded with a Bruker D8 powder diffractometer equipped with a SolX Si(Li) solid state detector using CuKα_1-Kα_2 radiation and a Göbel mirror. Intensities were recorded at 0.02° 2θ step intervals from 5 to 80°, with a 6 s counting time per step. Size of the divergence slit was 0.298°. Quantitative mineralogical compositions were determined by Rietveld refinement using Profex-BGMN programs (Doebelin and Kleeberg, 2015). JCPDS/ICDD and AMCD references used for the identification of the mineral phases are given in Table 1, and an example of Rietveld refinement made on XRD pattern of ore sample CT89 (red limonite) is shown in Fig. 4. Diffraction pattern and their repetitive fits are displayed in

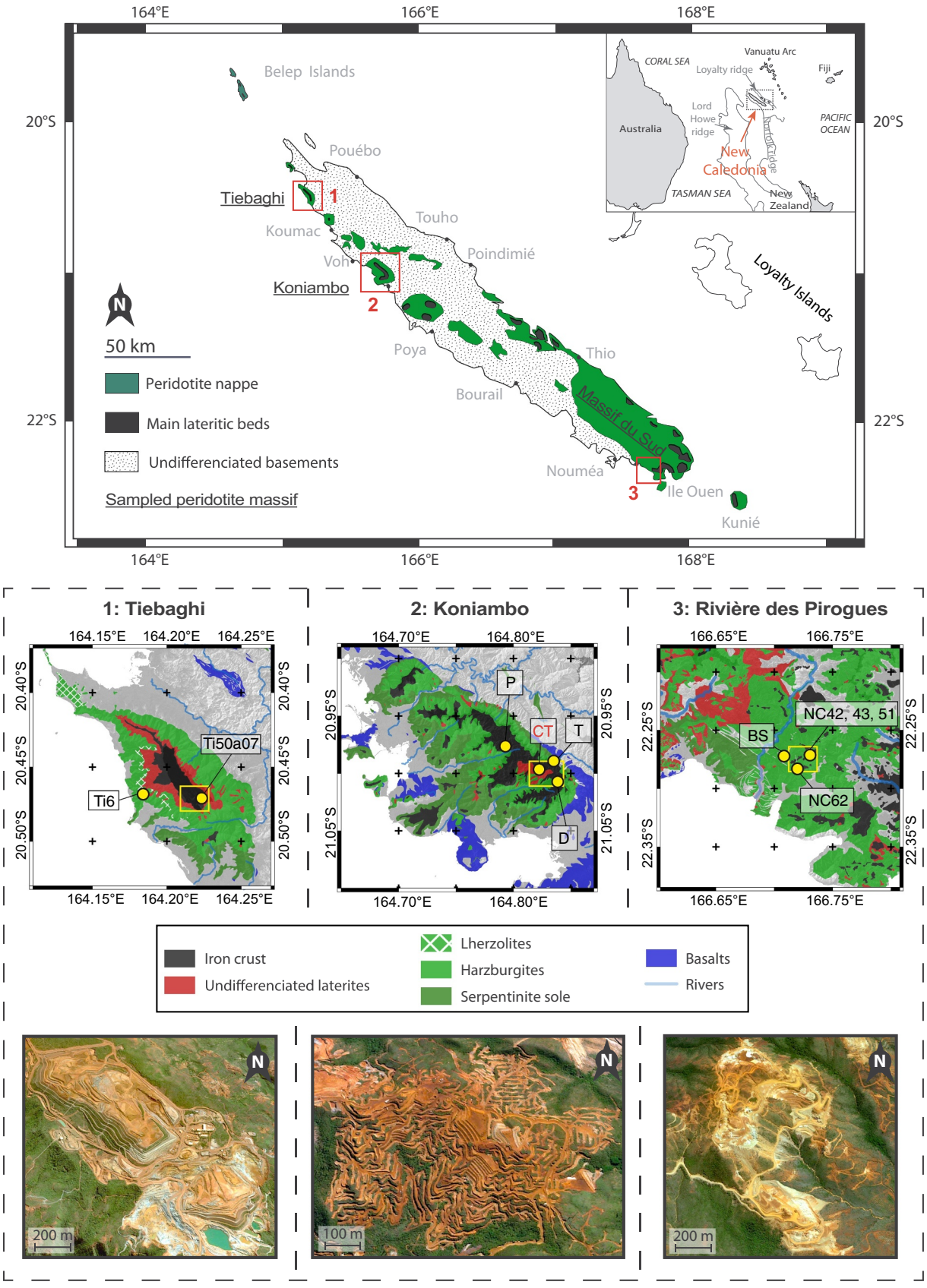

Fig. 1. Simplified geological maps of New Caledonia with the locations of the three massifs that were sampled during this study (data from DIMENC https://dimenc.gouv.nc/ressources/géologie). Yellow points indicate sampling locations, and satellite maps are located by yellow squares (Satellite maps are from Apple Maps® app). P: PIT207, T: Trazy, D: Doline, CT: Centre Trazy (in red, see Table 2, other samples and profiles are available in supplementary materials). (For interpretation of the references to colour in this figure legend, the reader is referred to the web version of this article.)

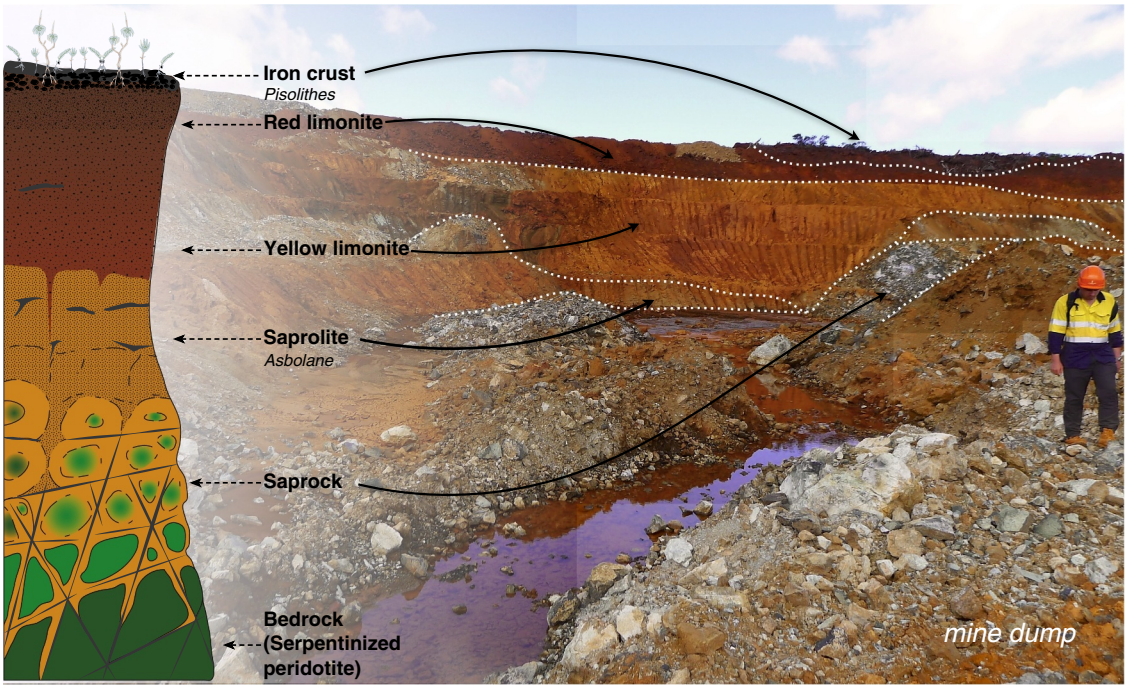

Fig. 2. Schematic representation of the typical weathering profile of New Caledonia Ni-laterites deposits and field photograph of Tiebaghi mine dump were the different weathering horizons can be observed.

supplementary materials. Since primary serpentines (mainly lizardite and chrysotile; Ulrich et al., 2014) can hardly be distinguished from secondary serpentines (lizardite, polygonal and Ni-serpentine; Cathelineau et al., 2016; Dublet et al., 2012) on the basis of XRD patterns and we therefore only refer to serpentine in Table 1 and XRD figures. In addition, the presence of Ni-Mg-talc-like belonging to the kerolite-pimelite series has been reported recently in the New Caledonia regolith (Cathelineau et al., 2015a, 2016; Fritsch et al., 2016; Muñoz et al., 2019). To date, the structure of this complex mineral phase is not yet fully determined. A Ni-Mg talc structure was therefore used for the structure refinement, with best fits obtained for 50% Mg substitution for Ni.

3.3. Raman spectroscopy

Raman spectra were acquired at Laboratoire GeoRessources (Vandoeuvre-lès-Nancy, France) using a Horiba Jobin-Yvon LabRam HR800 spectrometer and a visible ionized argon laser source with a wavelength of 659.43 nm. Output laser power of 100 mW was reduced to 0.8 mW using filter, and measurements were performed using an Olympus lens of 100× to focus the laser beam onto an area that was 1 µm in diameter. Analyses were carried out on 30 µm thick polished thin sections. Spectra result from the average of 4 acquisitions of 30 s to optimize the signal/noise ratio. Oxide species were determined by investigating the 200–900 cm^{-1} region of the Raman spectra.

3.4. Bulk rock chemistry

Major and trace element concentrations were determined at Service d'Analyses de Roches et Minéraux (SARM, Vandoeuvre-lès-Nancy, France) following the analytical procedure developed by Carignan et al. (2001). The complete procedure and detection limits are at the following address: http://helium.crpg.cnrs-nancy.fr/SARM/pages/roches.html.

3.5. In situ major and trace element analysis

Major elements analyses were performed using an electron

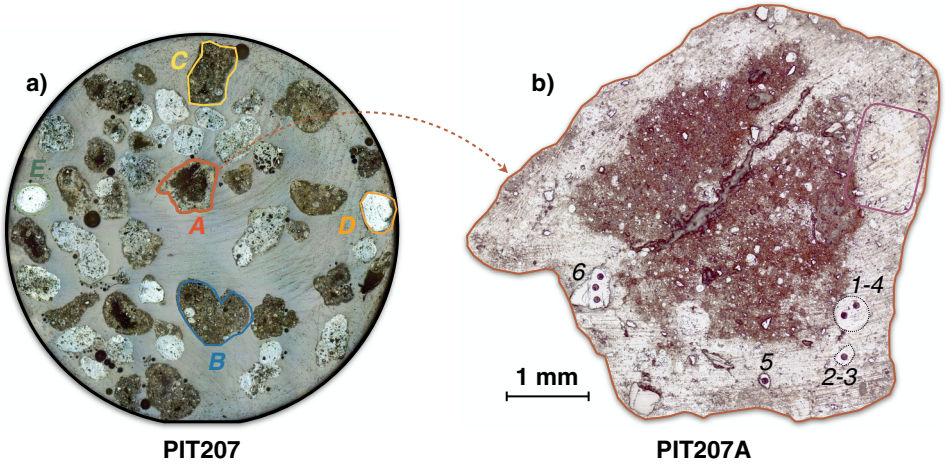

Fig. 3. a) Photograph of analyzed pisoliths from sample PIT207 (Koniambo Massif). **b)** Microphotograph of pisolith PIT207A. Numbers indicate in situ LA-ICP-MS analyzes reported in Table 4. The purple area corresponds to the chemical mapping area shown in Fig. 9 and in supplementary materials. (For interpretation of the references to colour in this figure legend, the reader is referred to the web version of this article.)

Table 1
Results of XRD-based mineral identification and quantification obtained by Rietveld refinement. Minerals with proportion < 1% have to be considered with caution, although the results of refinement were systematically better by taking these phases into account.

Minerals (%)	References	Bedrock	Saprock			Saprolite	Red limonite	Pisoliths
		CT31	CT21	CT19	CT15	CT41	CT89	CT90
Forsterite	JCPDS #01-077-1029	22.16	6.04	8.48	4.95	–	–	–
Enstatite	JCPDS #00-019-0768	5.90	4.30	1.58	–	–	–	–
Diopside	AMCSD 0000811	1.85	–	–	–	–	–	–
Serpentine	JCPDS #01-073-1336	59.29	65.70	42.67	23.40	–	–	–
Quartz	JCPDS #01-085-0798	–	10.91	12.99	14.25	35.95	0.12	0.87
Tremolite/actinolite	AMCSD 0001835/0001995	7.48	–	9.86	8.44	–	–	–
Talc-Ni	JCPDS #00-022-0711	–	1.26	6.10	29.94	20.08	2.54	0.82
Smectite	JCPDS #00-029-1491	1.77	0.94	0.86	6.59	–	–	1.30
Goethite	JCPDS #04-015-2898	–	8.61	16.35	12.43	39.39	76.15	34.67
Hematite	JCPDS #04-003-2900	–	–	–	–	2.72	4.90	51.36
Chromite	AMCSD 0006041	1.55	2.23	1.10	–	0.72	15.39	9.00
Lithiophorite	AMCSD 0001641	–	–	–	–	1.14	0.90	0.56
Gibbsite	JCPDS #00-029-0041	–	–	–	–	–	–	1.41
Total		100.00	99.99	99.99	100.00	100.00	100.00	99.99

microprobe analyser (EMPA) CAMECA SX100 at Service Commun de Microscopie Electronique et de Microanalyses (SCMEM, Vandoeuvre-lès-Nancy, France). Na, Mg, Al, Si, K, Ca, Ti, Cr, Mn, Fe, Ni were calibrated using natural and synthetic oxides as albite (Si, Na), corundum (Al), andradite (Ca), forsterite (Mg), hematite (Fe), $MnTiO_3$ (Mn, Ti), NiO (Ni), orthose (K). The operating conditions were: a current of 12 nA, an accelerating voltage of 15 kV, and a counting time of 10s. The beam diameter was focused to 1 µm. The total Fe is presented as Fe_2O_3. Chemical maps were obtained using the following operating conditions: 15 kV, 100 nA, dwell time of 100 ms and a step size of 2 µm (see supplementary materials). Phase maps were calculated using the approach developed in Muñoz et al. (2008) and adapted in Ulrich et al. (2014).

Trace element analyses were carried out using Laser Ablation Inductively Coupled-Plasma Mass Spectrometer (LA-ICP-MS) at Laboratoire GeoRessources composed of a 193 nm MicroLas ArF Excimer coupled with the Agilent 7500c quadrupole ICP-MS. Laser ablations were performed with a constant 5 Hz pulse rate, with an ablation crater of 44 to 90 µm in diameter. The number of pulses was fixed to 200, sufficient to form a long and stable signal for integration. The ablated material is transported using a He flow and mixed with Ar in a cyclone coaxial mixer prior to entering the ICP torch and being ionized. The following isotopes were measured: ^{45}Sc, ^{47}Ti, ^{51}V, ^{53}Cr, ^{55}Mn, ^{57}Fe, ^{59}Co, ^{60}Ni, ^{63}Cu, ^{66}Zn, ^{85}Rb, ^{88}Sr, ^{89}Y, ^{90}Zr, ^{93}Nb, ^{139}La, ^{140}Ce, ^{141}Pr, ^{146}Nd, ^{147}Sm, ^{153}Eu, ^{157}Gd, ^{159}Tb, ^{163}Dy, ^{165}Ho, ^{166}Er, ^{169}Tm, ^{172}Yb, ^{175}Lu, ^{181}Ta, ^{232}Th, ^{238}U. Internal standard were ^{29}Si and ^{57}Fe contents - previously determined by electron microprobe - respectively for the measurements of silicates and iron oxides. Concentrations were calibrated against the NIST SRM 610 rhyolitic glass using reference values from Jochum et al. (2011) for silicates and an in-house goethite standard especially developed during this study for iron oxides. Indeed,

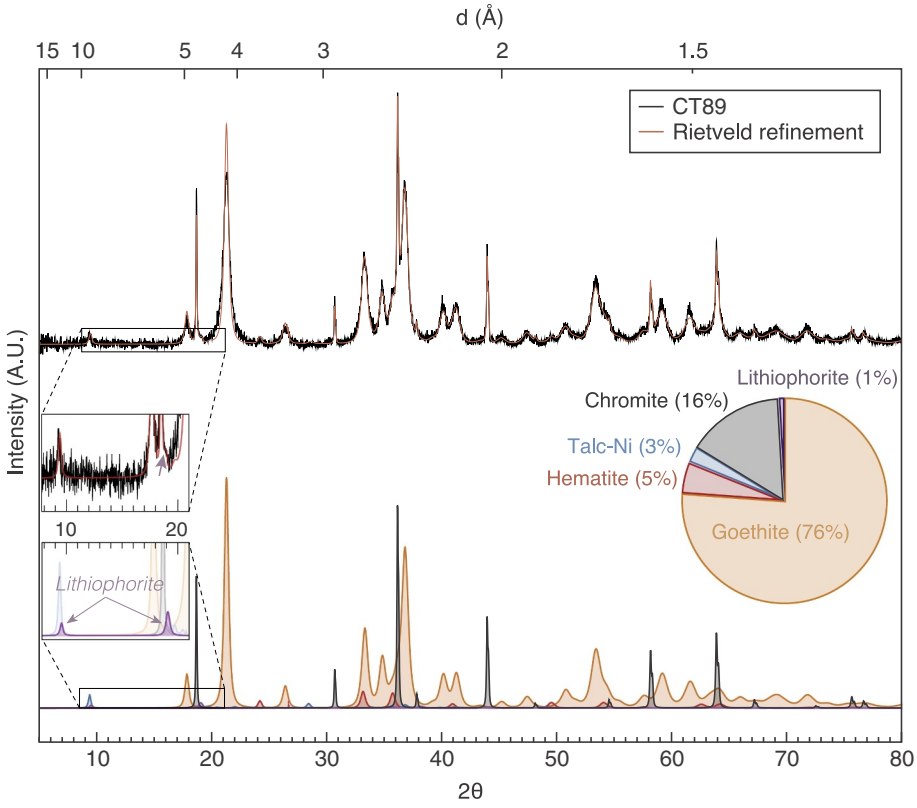

Fig. 4. XRD pattern of sample CT89 (red limonite, 2.5 m) and corresponding mineral phase identification and quantification based on Reitveld refinement (see also Table 1). Purple arrows show the presence of minor lithiophorite, highlighted by a small shoulder at the base of a chromite peak in the region near 19° (2Θ). Other XRD patterns are given in supplementary materials. (For interpretation of the references to colour in this figure legend, the reader is referred to the web version of this article.)

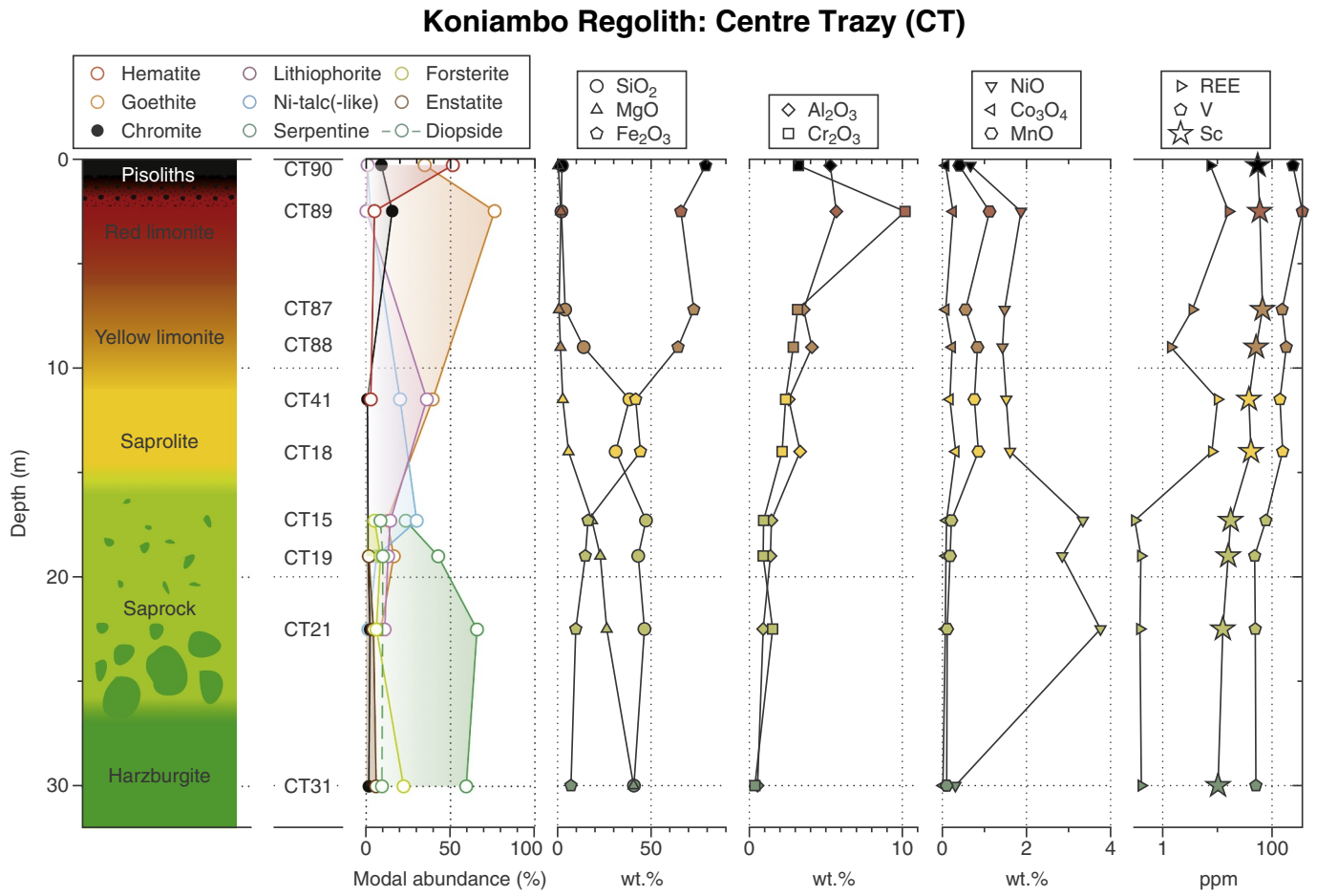

Fig. 5. Element distribution with depth of a typical lateritic regolith developed on the New Caledonia ophiolite. REE, V and Sc concentrations are shown on a logarithmic scale.

previous studies performing in situ trace element quantification on iron oxides used ^{57}Fe as internal standard and the silicate standard glass NIST SRM 610 for signal calibration (e.g. Aiglsperger et al., 2016; Green and Watling, 2007; Huelin et al., 2006). Same parameters were applied in this study during first in situ measurements of iron oxides, but preliminary results showed that for elements measured by both EMPA and LA-ICP-MS, concentrations determined by the latter were systematically greater (in the order of ~20–50%). This encouraged to prepare a specific standard (StdGoe 1.1) for iron oxides to limit matrix effects (standard preparation procedures and tests are developed in Appendix A at the end of this paper). Data reduction was carried out by using SILLS software (Guillong et al., 2008) and following the standard methods of Longerich et al. (1996).

4. Results

4.1. Mineralogy of the lateritic profile

Table 1 and Fig. 5 shows the results of mineral identification and quantification obtained for each horizon of the weathering profile by XRD and Rietveld refinements.

The mineralogy is typical of a lateritic profile development at the expense of an ultrabasic protolith (Butt and Cluzel, 2013 and references therein), and is consistent with previous results from Dublet et al. (2012, 2015) on the mineral proportions along the New Caledonia lateritic regolith: saprock is dominated by relicts of primary silicates (serpentine, olivine, enstatite, tremolite/actinolite) that are progressively replaced by secondary Mg-Ni-bearing silicates (which include serpentine, talc-like and smectite) and quartz. Iron oxides mainly consist of goethite and does not exceed 20%. However, goethite becomes the dominant mineral phase in saprolite (~41% in sample CT41), which also contains small amounts of hematite (< 3%) and Mn-oxides (asbolane and/or lithiophorite, ~1%). In this horizon, silicates are mainly quartz (~37%) and Ni-kerolite (~18%). The red limonite sample CT89 is almost exclusively composed of iron oxides (> 95%) of which > 75% are goethite. Other oxides are hematite (~5%), chromite (~16%) and Mn-oxides (< 1%). The same mineralogy is observed in pisoliths (sample CT90) with nevertheless a higher amount of hematite (~52%) compared to goethite (< 35%). Chromite represents ~10% of the sample and low amount of gibbsite ($Al(OH)_3$, < 2%) may occur. Relics of silicates, mainly quartz and talc-like, are systematically preserved even in the limonite horizons and ferricrete, although they represent < 5% of the mineralogy in these horizons.

4.2. Raman spectroscopic analysis of iron oxides in pisoliths

The discrimination between goethite and hematite is not obvious simply on the basis of optical microscopy. Therefore, Raman spectroscopy was systematically used to identify iron oxides in pisoliths prior further in situ geochemical investigations. Reference spectra used for comparison are from de Faria et al. (1997). Despite small differences in peak positions (< 5 cm^{-1}), there is good agreement between our results and reference spectra for all iron oxides (Fig. 6): goethite displays typical bands at 247, 299, 483, 559 and 680 cm^{-1}, the main peak being positioned at 393 cm^{-1}. Hematite is characterized by bands at 225, 293, 411, 502 and 613 cm^{-1}. An additional peak of a high intensity is

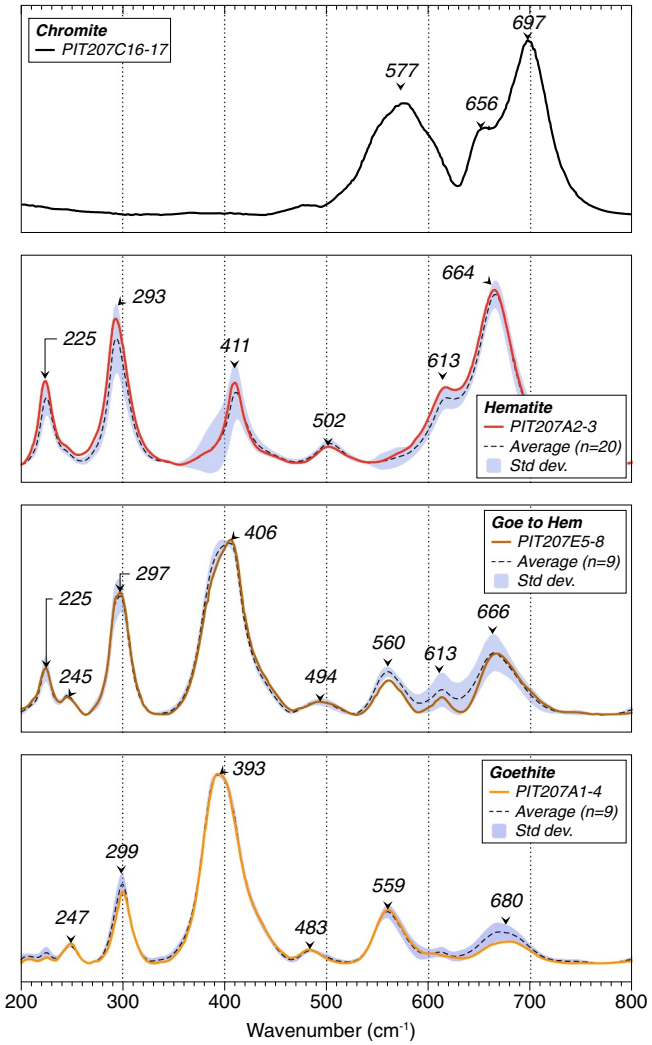

Fig. 6. Average Raman spectra of iron oxides (goethite, hematite, chromite) from pisoliths of PIT207 sample (Fig. 3). "Goe to Hem" corresponds to oxides with spectra that show an intermediate signal between that of goethite and hematite. Grey areas indicate the 2σ standard deviation. Intensities are in arbitrary units.

observed at 665 cm^{-1}. Such a high intensity, higher than the usual intensity observed for hematite at 293 cm^{-1}, may reflect important Fe-Al substitution (Zoppi et al., 2007). In addition, some oxides exhibit spectra with an intermediate signal between that of goethite and hematite, with a major peak ranging from 394 cm^{-1} (goethite) to 411 cm^{-1} (hematite), and additional bands centered around 225, 245, 297, 494, 560, 613 and 666 cm^{-1} (Fig. 6). The last iron oxide identified in pisoliths was the chromite inherited from magmatic assemblages, with a Raman spectra characterized by a broad band at 577 cm^{-1}, the main peak at 697 cm^{-1} with a shoulder at 656 cm^{-1}.

4.3. Geochemical evolution along the lateritic regolith

Fig. 5 and Table 2 show the geochemical evolution along the lateritic profile of Centre Trazy site (CT) sampled in the Koniambo massif. Other profiles are given in supplementary Table S1 and show comparable results to the CT profile. From bedrock to top, the profile is characterized by a progressive enrichment in Fe_2O_3 (7.13 to 79.2 wt%) and a depletion in MgO (40.6 to 0.34 wt%). SiO_2 remains relatively constant in bedrock and saprock (~43 wt%). It decreases from 38 wt% in saprolite down to 2.3 wt% in yellow and red limonites and pisoliths. A general observation is that SiO_2 is never completely depleted in the most weathered parts of the profile (i.e. red limonite and pisoliths/ferricrete) and has an average concentration of 2.62 wt% (0.57–8.57 wt %). Al_2O_3 and Cr_2O_3 show a typical enrichment of about 10 times from bedrock to pisoliths (0.54 to 5.29 and 0.36 to 3.21 wt%, respectively). Manganese and cobalt behave very similarly all along the profile: lowest concentrations are observed in the bedrock and the saprock (0.1–0.2 wt% MnO and 500–700 ppm Co), while their concentrations increase in the range of 0.5–1.2 wt% MnO (up to 3.65 wt%) and 1300–2300 ppm Co (up to 5600 ppm) in saprolite and yellow limonite. Both elements display lower concentrations in red limonite and pisoliths (< 0.7 wt% MnO and < 1000 ppm Co). Nickel concentration in the bedrock is low (~0.4 wt% NiO) but strongly increases in saprock, reaching 3–4 wt% NiO. In upper horizons, nickel behaves similarly to manganese and cobalt, with NiO concentrations between 1 and 1.5 wt% in limonites that decrease to ~0.5 wt% NiO in pisoliths. Vanadium behavior matches well those of aluminium and chromium: in the lateritic profile shown in Fig. 5, concentration in bedrock and saprock is ~50 ppm V, increasing from 140 ppm in saprolite to 241 ppm in pisoliths. Concentrations can be locally higher, reaching up to 360 ppm. Interestingly, this sample also contains the highest concentrations of Al_2O_3 and Cr_2O_3. Sc concentration progressively increases from bedrock (~10 ppm Sc in harzburgite) to limonites (usually ~80 ppm Sc) and correlates with Fe_2O_3. Highest Sc concentrations (up to 100 ppm Sc) are observed in samples with Fe_2O_3 ~70 ± 2 wt%, typically close to the transition between yellow and red limonites. At Fe_2O_3 > 75 wt %, corresponding to red limonite and/or pisoliths, Sc concentration almost systematically drops down (20–60 ppm Sc). Rare earth elements (REE) are extremely depleted in harzburgitic protolith (usually in the order of ppb) which exhibits a characteristic U-shaped pattern (Fig. 7; Allègre and Prinzhofer, 1985; Secchiari et al., 2016; Ulrich et al., 2011, 2010). As a consequence, total REE concentrations remain very low even in the limonite horizons where the highest concentrations are observed (ΣREE = 16–77 ppm). Only exceptions are from the two small profiles from the Bien-sûr mine where total REE concentrations can reach hundreds of ppm, which may reflect the proximity of weathered magmatic dikes. Elsewhere, saprock exhibits REE patterns similar to that of the bedrock, nevertheless with more enriched concentrations, although total REE do not exceed 1 ppm. Saprolite shows highly fractionated REE chondrite-normalized patterns, characterized by an enrichment in light REE (LREE) over heavy REE (HREE), and a strong Ce negative anomaly (Ce_N/Ce^* down to 0.067; Fig. 7 and supplementary Table S1). In this horizon, total REE concentrations vary from 1 to 10 ppm, with a low contribution of cerium. From yellow limonite to pisoliths, REE are increasingly depleted, with a slight depletion of LREE compared to saprolite and a positive Ce anomaly (Ce_N/Ce^* up to 5.64; Fig. 7 and supplementary Table S1). Total REE concentrations can reach several tens of ppm in these horizons, particularly in yellow limonite where the highest concentrations are generally observed, mainly due to strong contribution of cerium (up to 16 ppm Ce in sample MIA OPB7 4.0). Finally, a general observation is that REE accumulate in lateritic horizons where Mn, Co, and to a lesser extend Ni, are also significantly enriched (Fig. 5).

4.4. Mineral chemical compositions

Fig. 8 presents the concentrations of some transition metals (Sc, V, Cr, Mn, Co, Ni) in the different minerals that compose the bedrock (olivine, pyroxenes, serpentine, plagioclase, Table 3) on one hand and limonite and pisolith (goethite, hematite and chromite, which is residual from the bedrock; Table 4) on the other hand. Mn-oxides and relicts of silicates identified by XRD and EMPA measurements were too small to be analyzed by LA-ICP-MS, and their concentration in trace element were too low to be determined by EPMA. In the bedrock, highest Sc concentrations are measured in clinopyroxene (~60 ppm). Sc concentrations in orthopyroxene are lower (~31 ppm), and very low in other minerals composing the bedrock (5 ppm or less). Cr and V are

Table 2
Chemical composition of the Koniambo lateritic profile (site Centre Trazy, CT). Other profiles and samples are available in supplementary materials. n.d.: not determined; b.d.l.: below the limit of detection. UMIA is the ultramafic index of alteration, calculated as follow: UMIA = 100 × (Al2O3 + Fe2O3)/(SiO2 + MgO + Al2O3 + Fe2O3), and expressed in mol% (Aiglsperger et al. 2016). Major and trace element concentrations are in wt% and in ppm, respectively.

	CT90	CT89	CT87	CT88	CT41	CT18	CT15	CT19	CT21	CT31
Depth (m)	0.3	2.5	7.2	9.0	11.5	14.0	17.3	19.0	22.5	30.0
Location	Centre Trazy	Centre Trazy	Centre Trazy	Centre Trazy	Centre Trazy	Centre Trazy	Centre Trazy	Centre Trazy	Centre Trazy	Centre Trazy
Massif	Koniambo	Koniambo	Koniambo	Koniambo	Koniambo	Koniambo	Koniambo	Koniambo	Koniambo	Koniambo
Nature	Pisoliths	Red Laterite	Yellow Laterite	Yellow Laterite	Earthy Saprolite	Earthy Saprolite	Rocky Saprolite	Rocky Saprolite	Rocky Saprolite	Harzburgite
SiO_2	2.3	2.04	4.03	13.95	38.39	31.06	47.25	43.12	46.44	40.81
TiO_2	0.26	0.13	0.11	0.11	0.07	0.1	0.05	0.03	0.03	b.d.l.
Al_2O_3	5.29	5.69	3.55	4.09	2.58	3.32	1.44	1.38	0.9	0.54
Fe_2O_3	79.2	65.92	72.85	64.41	41.76	44.32	16.25	14.82	9.71	7.13
MnO	0.4	0.46	0.55	0.84	0.76	0.86	0.22	0.18	0.12	0.1
MgO	0.34	1.79	0.72	1.52	2.77	5.84	18.37	22.8	26.28	40.63
CaO	b.d.l.	0.05	b.d.l.	b.d.l.	b.d.l.	b.d.l.	0.22	0.54	b.d.l.	0.356
Na_2O	b.d.l.	0.02	0.01	0.01	0.07	0.08	0.03	0.05	0.01	b.d.l.
K_2O	b.d.l.	0.19	b.d.l.	b.d.l.	0.09	0.05	0.13	0.11	0.09	b.d.l.
P_2O_5	0.05	0.03	0.03	0.03	b.d.l.	b.d.l.	b.d.l.	b.d.l.	b.d.l.	b.d.l.
Cr_2O_3	3.21	10.18	3.15	2.87	2.37	2.14	0.93	0.9	1.52	0.36
NiO	0.67	2.04	1.48	1.43	1.52	1.61	3.34	2.85	3.76	0.31
LOI	7.91	11.14	13.45	11.01	10.28	11.12	12.3	12.83	11.62	9.78
Total	99.64	99.67	99.93	100.26	100.64	100.49	100.53	99.62	100.49	99.99
UMIA	91.10	87.4	83.6	58.3	25.1	29.6	8.5	8.01	4.95	3.38
Sc	54.5	59.7	66.9	51.1	37.7	41.1	17.5	15.8	12.6	10.3
V	241	358	153	182	140	156	77.1	48.1	49.3	50.6
Cr	21,993	69,683	21,570	19,646	16,197	14,650	6375	6190	10,431	2442
Co	574	1852	185	1710	1318	2329	734	626	515	98.5
Ni	5256	14,675	11,610	11,235	11,935	12,690	26,210	22,415	29,570	2406
Cu	34.4	77.2	36.5	29.6	22.7	39.8	22	6.29	864	1.08
Zn	251	995	277	400	212	358	226	143	797	35.9
Ga	7.98	5.22	3.23	3.54	2.16	2.63	2.03	1.06	0.259	n.d.
Ge	4.23	3.30	2.83	2.31	4.32	6.52	4.73	2.20	4.49	n.d.
As	8.98	1.54	4.61	8.71	b.d.l.	b.d.l.	b.d.l.	b.d.l.	1.5	b.d.l.
Rb	b.d.l.	0.392	b.d.l.	b.d.l.	0.495	b.d.l.	0.303	b.d.l.	b.d.l.	0.185
Sr	b.d.l.	b.d.l.	b.d.l.	b.d.l.	b.d.l.	b.d.l.	5.69	2.71	2.49	0.752
Y	1.29	2.22	0.848	0.811	2.07	2.08	0.267	0.15	b.d.l.	0.053
Zr	22.7	2.11	1.6	1.47	1.2	1.01	3.23	b.d.l.	b.d.l.	0.113
Nb	0.728	0.113	b.d.l.	b.d.l.	b.d.l.	b.d.l.	0.092	b.d.l.	b.d.l.	0.023
Mo	2.34	0.67	0.557	b.d.l.	b.d.l.	b.d.l.	0.843	0.669	0.756	b.d.l.
Cd	b.d.l.	0.32	b.d.l.	b.d.l.	b.d.l.	0.205	0.43	0.397	0.302	b.d.l.
In	0.273	b.d.l.	0.228	0.113	0.102	0.11	0.204	b.d.l.	b.d.l.	b.d.l.
Sn	0.719	0.453	0.467	b.d.l.	b.d.l.	0.739	b.d.l.	0.641	2.05	b.d.l.
Sb	b.d.l.	b.d.l.	b.d.l.	b.d.l.	b.d.l.	b.d.l.	0.31	b.d.l.	b.d.l.	b.d.l.
Cs	b.d.l.	b.d.l.	b.d.l.	b.d.l.	0.116	b.d.l.	b.d.l.	0.138	b.d.l.	0.006
Ba	11.1	49.2	10.0	3.44	4.75	7.12	5.88	9.00	14.9	0.24
La	0.459	1.27	0.35	0.254	1.43	2.03	0.115	b.d.l.	0.14	0.024
Ce	5.70	11.6	4.07	0.335	1.01	0.356	b.d.l.	0.202	0.175	0.056
Pr	0.128	0.275	0.181	0.06	0.933	0.807	0.016	0.017	0.015	0.007
Nd	0.472	1.21	0.86	0.25	4.04	3.03	0.064	0.063	b.d.l.	0.029
Sm	0.119	0.35	0.286	0.066	0.493	0.126	0.018	0.02	b.d.l.	0.006
Eu	0.031	0.083	0.069	0.021	0.119	0.041	0.008	b.d.l.	b.d.l.	0.001
Gd	0.133	0.407	0.198	0.08	0.606	0.495	0.02	0.018	b.d.l.	0.006
Tb	0.024	0.055	0.036	0.015	0.069	0.03	0.005	b.d.l.	b.d.l.	0.001
Dy	0.132	0.286	0.19	0.093	0.437	0.228	0.014	0.017	0.014	0.007
Ho	0.027	0.065	0.032	0.02	0.1	0.075	0.002	0.005	0.003	0.001
Er	0.08	0.191	0.086	0.068	0.338	0.276	0.011	0.013	0.013	0.007
Tm	0.017	0.038	0.016	0.014	0.05	0.037	0.004	0.004	0.001	0.235
Yb	0.105	0.241	0.122	0.122	0.428	0.334	0.028	0.036	0.023	0.009
Lu	0.02	0.043	0.015	0.022	0.096	0.111	0.008	0.008	b.d.l.	0.002
Hf	0.687	0.043	0.03	0.035	0.03	b.d.l.	0.071	b.d.l.	b.d.l.	0.003
Ta	0.063	b.d.l.	b.d.l.	b.d.l.	0.01	b.d.l.	b.d.l.	b.d.l.	b.d.l.	b.d.l.
Pb	6.67	8.65	4.97	2.32	1.60	1.78	3.96	2.41	16.3	0.063
Bi	0.329	0.133	b.d.l.	b.d.l.	b.d.l.	0.118	0.142	0.121	0.466	n.d.
Th	0.918	0.071	0.078	0.03	0.086	b.d.l.	b.d.l.	0.09	0.062	0.008
U	0.324	0.235	0.059	0.084	0.114	0.076	b.d.l.	0.057	0.042	0.005

mainly concentrated in chromite, but significant concentrations are also observed in pyroxenes (in average, 7474 ppm Cr and 241 ppm V in Cpx; 5331 ppm Cr and 126 ppm V in Opx). In olivine, serpentine and plagioclase, Cr and V contents are low (< 100 ppm Cr and < 5 ppm V). Highest Mn concentrations are measured in plagioclase (3563–6660 ppm Mn). In other minerals, Mn concentrations are highly variable, ranging from 77.4 to 1394 ppm in clinopyroxene, 542 to 1432 ppm in orthopyroxene, 310 to 1626 ppm in olivine and 271 to 426 ppm in serpentine. Main Co and Ni carriers are olivine and serpentine (~150 ppm Co and ~3500 ppm Ni), while concentrations in pyroxenes are lower (66.1 ppm Co, 957 ppm Ni in average in Opx; 27.6 ppm Co, 471 ppm Ni in average in Cpx).

In pisoliths, results of in situ measurements show that iron oxides contain relatively high amount of transition metals compared to initial

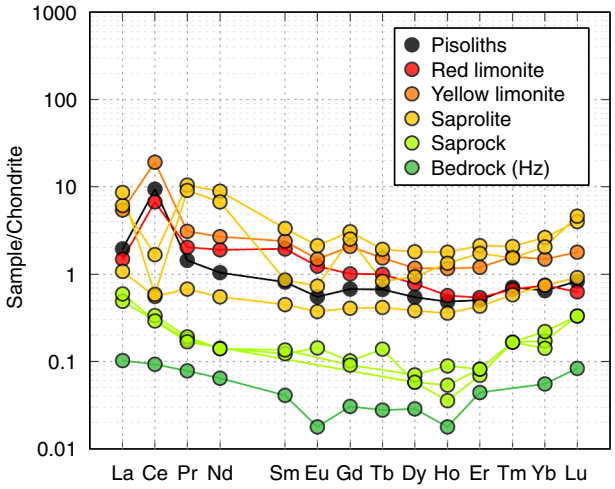

Fig. 7. Chondrite-normalized REE patterns of bedrock, saproliths, limonites and pisoliths samples from Table 2. Chondrite values are from Anders and Grevesse (1989).

concentrations in silicates. Highest Sc concentrations are observed in goethite (82.7 ppm Sc in average, up to 136 ppm). Hematite contains substantially lower amount of scandium (47.5 ppm Sc in average, up to 76.6 ppm). Vanadium and chromium are mainly hosted by chromite (~980 ppm V and > 46 wt% Cr_2O_3), but also redistributed in goethite and hematite (~250 ppm V and ~3.50 wt% Cr_2O_3). Sc concentration is rather low in chromite (< 2 ppm Sc), as other transition metals (Mn, Co, Ni, Cu) compared to concentrations in goethite and hematite, with exception of Zn (1463 ppm in chromite vs. 320 ppm in goethite and 287 ppm in hematite, in average). The highest concentrations in manganese, nickel and cobalt are mainly observed in relicts of Mn-oxides, with concentrations up to 38.79 wt%, 23.35 wt% and 10.83 wt%, respectively (Figs. 8 and 9). However, goethite and hematite display significant concentrations in these metals, which can reach several thousand of ppm (661–4652 ppm Mn, 34.8–1860 ppm Co, 1776–7082 ppm Ni in goethite, 468–6479 ppm Mn, 61.4–1784 ppm Co, 1752–6242 ppm Ni in hematite).

5. Discussion

5.1. Relation between mineralogy and enrichments in transition and critical metals along the weathering profile

First order calculations have been performed in order to identify the main bearing phases for a set of transition metals (i.e. Sc, V, Cr, Mn, Co and Ni) along the CT weathering profile. The approach for such calculations is based on the combination of, i) the modal abundance of minerals obtained from Rietveld refinements of XRD patterns (see Table 1 and Fig. 5), and ii) the chemical compositions of minerals identified in the bedrock and in the pisolith (i.e. determined by EPMA and LA-ICP-MS; see Tables 3 and 4), assuming the fact that minor/trace element composition for each of these minerals remains constant along the regolith. On this basis, it is possible to calculate the bulk concentration in the latter elements for each weathered horizon (Fig. 10). The close match observed between “calculated bulk analyses” and “measured bulk analyses” (i.e. Table 2 and Fig. 5) demonstrate the relevance of the approach. On the left side of bulk rock curves, the percentage of specific element-bearing minerals required to reach bulk concentration is displayed. Results obtained for each element are discussed hereafter. It is worth noting that even if this modeling is limited to a single profile, we consider it as representative of the NC regolith since geochemical and mineralogical evolutions with depth are very similar to those that can be found in the literature (e.g. Dublet et al., 2015)

5.1.1. Nickel

Our calculations show that the main contribution to Ni in the bed rock are serpentine (~75%) and olivine (~25%), while in the rocky saprolite horizon is mainly hosted by serpentine (up to 90%). At the top of rocky saprolite, the proportion of Ni hosted by serpentine decreases down to 20%, while more and more Ni is hosted by Ni-talc-like, as characterized by Muñoz et al. (submitted), which is the main Ni carrier up to the top of the earthy saprolite horizon with ~85% of total Ni (Fig. 10). It is worth noting that our calculated Ni concentrations are too high compared to the bulk concentrations in the rocky-to-earthy saprolite domain. This misfit may be related to an overestimation of the Ni content in Ni-talc-like: a concentration of ~10,000 ppm Ni was used for Ni-talc-like in our calculation, corresponding to ~20 wt% NiO in agreement with a value reported by Cathelineau et al. (2016), but Ni-kerolite may contain highly variable amount of nickel in its structure since it likely corresponds to a Mg-Ni solid solution that is about to strongly evolve in composition in regard with the degree of weathering (Muñoz et al., submitted). In the lateritic units, nickel that is likely released by the dissolution of Ni-bearing phyllosilicates is incorporated into iron oxides. Consistently with results previously published by Dublet et al. (2015, 2012), nickel is mainly hosted by goethite which contains ~40% of the bulk Ni content in laterite, likely by substituting Fe^{3+} in the mineral structure (Singh et al., 2002) and/or by being adsorbed at the oxide surface (e.g. Beukes et al., 2000). Even so, the relicts of silicates may still contribute significantly to the total Ni budget of laterites (up to 38% in sample CT89, Fig. 10). Mn-oxides only contribute to < 18% of the total Ni budget in laterites, which is in agreement with previous estimations based on X-ray absorption spectroscopy (< 20%; Dublet et al., 2012). At the very top of the profile (i.e. in the ferricrete), Ni appears to be mainly hosted by hematite (35%) and goethite (28%), as well as some residual silicates (~3%).

5.1.2. Manganese and cobalt

Manganese and cobalt display very similar behavior along the weathering profile. Both are mainly hosted by olivine and serpentine minerals in the peridotite. In a less extent, pyroxenes can contain several hundreds of ppm of Mn. Since chromite contains ~1000 ppm Mn and occurs all along the weathering profile, it contributes to ± 5% of the total Mn budget in the different units. In saproliths, Mn and Co released after the dissolution of the primary silicates are integrated into newly formed, and likely poorly crystallized goethite, by a combination of adsorption and replacement of iron in the oxide structure (Gerth, 1990; Singh et al., 2002). At the transition between saprolite and yellow limonite, manganese and cobalt are mainly concentrated in Mn-oxides (mainly asbolane and lithiophorite with minor birnessite; Butt and Cluzel, 2013; Fandeur et al., 2009b; Llorca and Monchoux, 1991; Manceau et al., 1987; Nahon and Parc, 1990). Based on the study of Marker et al. (1991, and references therein), the formation of Mn-oxides in such context derives from the leaching of Mn and Co from the near-surface parts of the weathering profile, forming Mn colloidal complexes that precipitate due to pH rising and supersaturation of the solution. At the upper levels, with decreasing pH and relative humidity, the combination of CO_2 and bacterial activities leads to the dissolution of Mn-oxides and reduction of Mn (Quantin et al., 2002). Fractions of Mn and Co released from dissolving Mn-oxides may be incorporated in iron oxides, although most of them are leached downwards. As a consequence, Mn and Co are depleted in the upper horizons where they are mainly hosted by goethite and hematite (Fig. 10).

5.1.3. Chromium and vanadium

Among minerals that compose the bedrock, chromite contains by far the highest concentrations of chromium and vanadium. Chromite is highly resistant to weathering, although it may suffer from slight

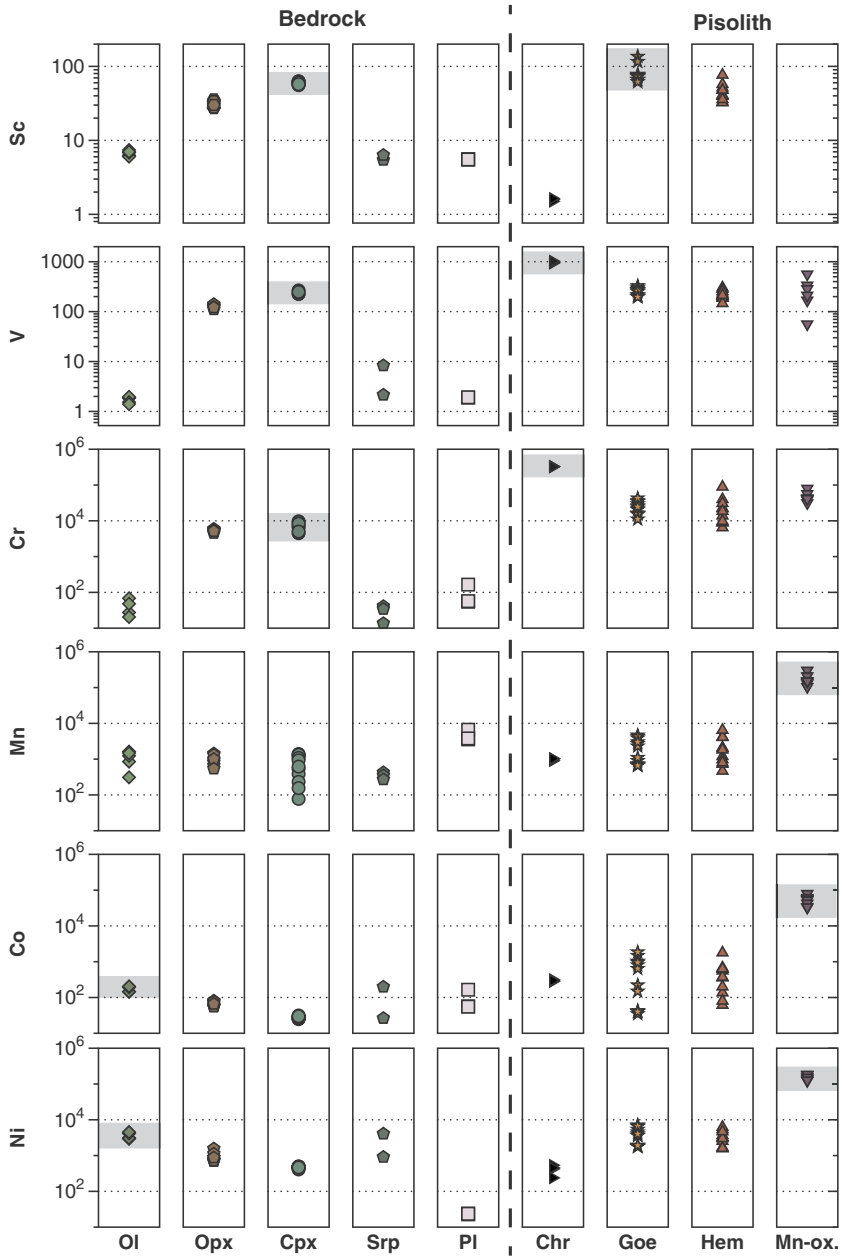

Fig. 8. Concentrations of critical and transition metals (Sc, V, Cr, Mn, Co, Ni) in minerals that compose the bedrock (Ol: olivine; Opx: orthopyroxene; Cpx: Clinopyroxene; Pl: plagioclase) and pisoliths (Chr: chromite; Goe: goethite; Hem: hematite; Mn-ox.: Mn-oxides). Mineral concentrations were measured by LA-ICP-MS with exception of Mn-oxides which were too small and for which concentrations were determined by EPMA (in that case, most of trace elements, i.e. Sc, Ti, V, Cu, Zn were below the detection limit of EPMA).

supergene dissolution at the uppermost parts of the profile (Traore et al., 2008). Therefore, we observe an excellent correlation between the concentration in Cr and V and the amount of chromite along the lateritic profile. Our calculations show that Cr and V released from the progressive dissolution of pyroxenes in the bedrock and saprock are trapped by goethite. Both elements being likely in their reduced form, i.e. trivalent, they easily substitute Fe(III) in the structure of goethite and hematite although fractions of Cr may be also adsorbed at mineral surface (Fandeur et al., 2009a, 2009b; Oze et al., 2004; Schwertmann and Latham, 1986; Schwertmann and Pfab, 1996). Locally, in the presence of Mn-oxides, Cr is oxidized to Cr^{6+} (Fandeur et al., 2009b; Oze et al., 2004). In this form, Cr is assumed to be highly mobile, but according to Fandeur et al. (2009b), Cr^{6+} is immediately re-adsorbed onto surrounding goethite after oxidation by Mn-oxides. As a consequence, Cr and V concentrations increase along the lateritic profile towards the surface and can be considered as immobile and mainly controlled by primary chromite and secondary iron oxides (Fig. 10).

5.1.4. Scandium

Although they represent < 20% of the mineralogy in the bedrock, we show that pyroxenes host the almost total amount of scandium (Figs. 8 and 10). The dissolution of these pyroxenes leads to the release of Sc that subsequently concentrates into newly formed goethite: in saprock, our calculations show that > 60% of Sc is hosted by goethite, which represents < 15% of the paragenesis in this horizon. In overlying limonites, the amount of Sc associated to goethite increases up to ~95%, before decreasing to 50% in the pisolith horizon in which Sc is hosted for a half by hematite. In this case, bulk Sc concentrations are systematically lower, reflecting that fractions of Sc may be mobilized during the development of hematite at the expense of goethite (see

Table 3
Chemical composition of bedrock minerals. b.d.l.: below the limit of detection; n.d.: not determined. Major and trace element concentrations are in wt% and in ppm, respectively. Trace element in italic are calculated from major element concentrations.

	Clinopyroxene	Std dev.	Orthopyroxene	Std dev	Olivine	Std dev	Serpentine	Std dev	Plagioclase	Std dev
	Average (n = 11)		Average (n = 8)		Average (n = 5)		Average (n = 3)		Average (n = 3)	
SiO_2	53.00	0.67	56.09	0.70	41.28	0.14	42.15	1.19	36.67	0.22
TiO_2	0.13	0.02	0.05	0.02	b.d.l.		0.01	0.01	0.05	0.02
Al_2O_3	3.13	0.98	3.37	0.82	b.d.l.		0.17	0.17	21.95	0.19
FeO	2.18	0.18	4.72	0.24	7.43	0.34	3.97	1.78	1.06	0.86
MnO	0.09	0.06	0.12	0.04	0.14	0.07	0.05	0.01	0.6	0.22
MgO	18.2	0.67	33.62	1.48	51.82	0.26	40.35	1.9	0.83	0.47
CaO	22.83	0.74	1.86	1.68	0.03	0.02	0.01	0.01	35.99	1.68
Na_2O	0.23	0.10	0.09	0.13	0.04	0.03	0.02	0.02	0.03	0.03
K_2O	0.02	0.01	0.09	0.14	0.02	0.01	0.01	0.01	b.d.l.	
Total	99.81	3.42	100.01	5.25	100.74	0.4	86.73	1.53	97.17	0.51
Trace elements										
Sc	59.9	2.34	31.1	3.3	6.71	0.556	5.74	0.517	5.53	0.036
Ti	*777*	*146*	*276*	*130*			*69.9*	*45.8*	*270*	
V	241	12.6	126	9.77	1.73	0.241	4.21	3.58	1.91	0.025
Cr	7474	1643	5331	423	41.1	21.6	29.6	14.2	92.3	63.3
Mn	725	488	957	327	1100	529	349	77.4	4673	1725
Co	27.6	1.98	66.1	10.5	167	29.4	142	99.7	92.2	62.6
Ni	471	23.6	922	293	3556	719	3022	1827	23.4	0.653
Rb	b.d.l.		b.d.l.		b.d.l.		b.d.l.		b.d.l.	
Sr	0.416	0.394	0.282	0.245	b.d.l.		b.d.l.		b.d.l.	
Y	10.8	3.05	1.18	0.274	b.d.l.		b.d.l.		b.d.l.	
Zr	0.498	0.239	0.135	0.020	b.d.l.		b.d.l.		b.d.l.	
Nb	0.079	0.016	b.d.l.		b.d.l.		b.d.l.		b.d.l.	
La	b.d.l.		b.d.l.		b.d.l.		b.d.l.		b.d.l.	
Ce	b.d.l.		b.d.l.		b.d.l.		b.d.l.		b.d.l.	
Pr	b.d.l.		b.d.l.		b.d.l.		b.d.l.		b.d.l.	
Nd	0.069	0.022	b.d.l.		b.d.l.		b.d.l.		b.d.l.	
Sm	0.241	0.059	b.d.l.		b.d.l.		b.d.l.		b.d.l.	
Eu	0.131	0.036	0.021	0.022	b.d.l.		b.d.l.		b.d.l.	
Gd	0.726	0.177	0.019	0.016	b.d.l.		b.d.l.		b.d.l.	
Tb	0.207	0.046	0.015	0.002	b.d.l.		b.d.l.		b.d.l.	
Dy	1.82	0.426	0.155	0.071	b.d.l.		b.d.l.		b.d.l.	
Ho	0.432	0.107	0.046	0.018	b.d.l.		b.d.l.		b.d.l.	
Er	1.32	0.317	0.177	0.066	b.d.l.		b.d.l.		b.d.l.	
Tm	0.201	0.055	0.041	0.021	b.d.l.		b.d.l.		b.d.l.	
Yb	1.62	0.322	0.21	0.081	b.d.l.		b.d.l.		b.d.l.	
Lu	0.209	0.043	0.055	0.018	b.d.l.		b.d.l.		b.d.l.	
Ta	b.d.l.		b.d.l.		b.d.l.		b.d.l.		b.d.l.	
Th	b.d.l.		b.d.l.		b.d.l.		b.d.l.		b.d.l.	
U	b.d.l.		b.d.l.		b.d.l.		b.d.l.		b.d.l.	

Section 5.2 below). In other mineral phases such as chromite or silicate relics, Sc concentration is too low to contribute significantly to the bulk rock Sc budget. Although we were not able to determine Sc content of Mn-oxides during this study, it may be assumed to be very low by considering the evolution of bulk rock concentrations along with depth in the regolith (Fig. 5 and supplementary materials): Indeed, the presence of Mn-oxides in samples is highlighted by an increase of Mn, Co and REE concentrations, but no significant Sc anomaly was detected. To date, only a few of studies have investigated the Sc speciation in lateritic deposits. First data were provided by Chassé et al. (2017) who proposed a study of the lateritic profile of the Syerston–Flemington deposit (Australia), which developed on an ultramafic-mafic intrusive complex. They concluded that Sc is adsorbed on goethite and incorporated in the crystal structure of hematite by substituting Fe^{3+}. In parallel, a communication by Muñoz et al. (2017) providing a further study of Sc speciation in New Caledonia laterites by coupling X-ray absorption spectroscopy and sequential chemical extraction, demonstrate that Sc is actually mainly integrated in the structure of goethite rather being adsorbed.

5.1.5. Rare-earth elements

The linear enrichment in lanthanides observed during the saprolitization stage of weathering indicates a residual enrichment (Fig. 7). However, the high REE concentrations characterizing the top of saprolite are not consistent with a linear, residual enrichment but rather highlight an external contribution (Fig. 5). This enrichment coincides with LREE fractionation, strong negative Ce anomaly ($Ce_N/Ce^* << 1$) and high Mn-Co concentrations (Figs. 5 and 7). At the opposite, upper levels show lower REE concentrations with a positive Ce anomaly ($Ce_N/Ce^* > 1$). All these observations illustrate the mobilization of REE at the interface between saprolite and limonite. Such mobility has been previously described in other lateritic profiles worldwide (e.g. Aiglsperger et al., 2016; Braun et al., 1990; Dequincey et al., 2002; Dequincey et al., 2006; Janots et al., 2015; Marker et al., 1991; Marsh, 1991). REE released by the weathering of primary silicates (mostly pyroxenes) are mainly adsorbed by secondary amorphous or poorly crystallized Fe-hydroxides (Ohta and Kawabe, 2001). The progressive ordering of the crystal structure of goethite from these amorphous precursors occurs via successive ageing and dissolution-reprecipitation reactions that decreases the sorption capacity of the mineral (Dublet et al., 2015; Koeppenkastrop and De Carlo, 1992; Schwertmann and Murad, 1983). Such decreases of sorption capacity may lead to the progressive release of REE by goethite with increasing weathering. The close link between REE and Mn-Co enrichments is consistent with the scavenging of REE by Mn-oxides (Aiglsperger et al., 2016; Braun et al., 1990; Janots et al., 2015; Koeppenkastrop and De Carlo, 1992; Ohta and Kawabe, 2001; Pourret and Davranche, 2013). In addition, REE sorption on Mn-oxides may be the cause of Ce-oxidation (Bau et al.,

Table 4
Composition of major elements and transition metals iron oxides in Pisoliths of PIRA and PIT207 samples. For Mn-oxides and silicates, trace element concentrations correspond to concentrations of major elements in wt% converted into ppm. b.d.l.: below the limit of detection; n.d.: not determined.

	Goethite													
	PIRA-B4	PIRA-C1	PIRA-C2	PIRA-C3	PIRA-C4	PIRA-D1-1	PIT207A1-4	PIT207B10-14	PIT207C5-8	PIT207C9-10	PIT207C15	PIT207E5-8	Average (n = 12)	Std dev.
SiO_2	4.22	3.55	3.82	3.58	3.56	5.72	1.66	1.27	2.86	1.74	1.67	3.43	3.09	1.31
TiO_2	0.14	0.48	0.26	0.49	0.35	0.10	0.20	0.16	0.07	0.09	0.17	0.11	0.22	0.15
Al_2O_3	5.52	10.73	10.52	3.43	11.50	5.30	6.82	7.21	7.13	4.20	4.53	3.95	6.74	2.81
Fe_2O_3	73.88	66.49	70.11	75.76	70.58	74.75	76.79	76.19	75.15	72.74	76.00	76.58	73.75	3.19
MnO	0.12	0.09	0.09	0.09	0.09	0.14	0.29	b.d.l.	b.d.l.	b.d.l.	b.d.l.	b.d.l.	0.13	0.07
MgO	0.48	0.54	0.62	0.49	0.44	0.74	0.07	b.d.l.	b.d.l.	b.d.l.	b.d.l.	b.d.l.	0.48	0.21
CaO	0.11	0.12	0.12	0.11	0.07	0.09	b.d.l.	b.d.l.	b.d.l.	b.d.l.	b.d.l.	b.d.l.	0.10	0.02
Cr_2O_3	2.38	3.24	2.31	3.00	2.21	1.62	3.60	3.89	3.43	8.68	5.53	4.44	3.69	1.90
NiO	0.46	0.22	0.23	0.24	0.24	0.58	0.69	0.70	1.33	0.63	b.d.l.	b.d.l.	0.53	0.34
Total	87.31	85.46	88.09	87.20	89.04	89.03	90.12	89.41	89.97	88.08	87.91	88.51	88.44	1.31
Trace elements														
Sc	66.0	74.4	73.4	77.8	73.0	66.8	77.6	76.4	136	72.5	116	81.7	82.7	21.3
Ti	830	2869	1577	2918	2112	576	1209	960	415	525	1044	653	1307	882
V	200	273	307	328	293	216	249	214	201	274	260	196	251	45.4
Cr	16,276	22,169	15,822	20,501	15,147	11,056	36,415	29,661	26,059	34,057	42,852	24,573	24,549	9685
Mn	900	671	695	732	661	1105	2700	2295	3853	4652	4264	3013	2128	1534
Co	222	41.1	34.8	42.4	39.9	149	1480	805	640	1022	1859	955	607	626
Ni	3645	1756	1817	1905	1918	4526	5363	3602	7083	6473	6688	4017	4066	1994
Cu	24.8	35.6	36.0	40.3	42.4	14.3	33.7	21.5	20.4	23.8	21.5	20.6	27.9	9.18
Zn	507	245	256	266	277	261	412	396	225	304	422	271	320	90.2

	Hematite													Chromite					
	PIRA-A1	PIRA-A2a	PIRA-A3	PIRA-A4b	PIRA-B1	PIT207A2-3	PIT207B6-7	PIT207C1-4	PIT207C12-13	PIT207E2-4	PIT207E9-11	Average (n = 11)	Std dev.	PIT207A5	PIT207A6	PIT207C16-17	PIT207E1	Average (n = 4)	Std dev.
SiO_2	3.51	2.71	3.82	2.44	3.36	1.98	0.99	1.52	0.86	1.18	1.43	2.16	1.07	0.14	0.36	0.52	0.12	0.28	0.19
TiO_2	0.43	0.37	0.29	0.38	0.21	0.11	0.36	0.24	0.20	0.24	0.21	0.28	0.10	0.02	b.d.l.	0.02	b.d.l.	0.02	
Al_2O_3	13.41	12.70	13.34	12.93	5.23	3.96	3.02	4.69	2.10	3.79	2.76	7.08	4.84	24.60	23.70	24.25	24.18	24.18	0.37
Fe_2O_3	78.59	79.10	80.48	78.95	87.85	91.20	88.25	86.62	87.90	88.62	91.95	85.41	5.10	14.51	14.67	13.47	15.30	14.49	0.76
MnO	0.17	0.07	0.55	0.11	0.16	0.35	0.22	0.06	1.08	0.11	0.30	0.29	0.30	0.12	0.17	0.13	0.17	0.15	0.03
MgO	0.51	0.29	1.09	0.50	0.57	0.23	0.34	0.03	0.19	0.43	0.15	0.39	0.29	13.33	14.10	13.53	13.95	13.73	0.36
CaO	0.08	0.09	0.09	0.12	0.04	b.d.l.	b.d.l.	b.d.l.	b.d.l.	b.d.l.	b.d.l.	0.08	0.03	b.d.l.	b.d.l.	b.d.l.	b.d.l.	b.d.l.	
Cr_2O_3	2.28	3.62	0.95	3.77	1.64	1.47	6.07	6.45	7.25	5.19	3.29	3.82	2.17	46.76	47.53	48.42	46.99	47.43	0.74
NiO	0.25	0.22	0.32	0.24	0.51	0.64	0.73	0.76	0.25	0.61	0.44	0.45	0.21	0.07	0.09	0.03	0.06	0.06	0.03
Total	99.23	99.16	100.94	99.43	99.56	99.93	99.98	100.37	99.82	100.16	100.54	99.92	0.56	99.55	100.62	100.36	100.77	100.32	0.54
Trace elements																			
Sc	39.7	41	51.6	33.2	47.8	32.4	40.3	57.3	54.9	76.6	47.9	47.5	12.7	1.59	1.5	1.64	b.d.l.	1.57	0.071
Ti	2261	2021	1744	1969	987	658	2646	1420	1181	1446	1233	1597	591	23.8	25.7	12.9	5.61	17	9.45
V	193	202	206	186	146	229	302	284	211	253	213	221	44.8	971	985	939	1024	980	35.2
Cr	13,833	22,597	6467	22,123	8955	8899	39,752	48,786	49,752	30,820	18,589	24,597	15,710	323,571	325,213	333,561	321,519	325,966	5284
Mn	1198	468	4235	729	971	2088	4082	800	6479	1996	1827	2261	1892	908	1033	1018	1038	999	61.2
Co	136	61.4	357	80.5	200	559	622	373	1784	681	636	499	484	282	285	316	298	295	15.3
Ni	1710	1572	2518	1601	3202	3238	3683	5383	6242	2999	4681	3348	1554	535	427	238	456	414	126
Cu	24.3	20.3	36.3	24.0	20.3	5.23	6.36	b.d.l.	27.2	5.52	b.d.l.	18.8	10.93	3.37	3.21	b.d.l.	b.d.l.	3.29	0.115
Zn	367	339	501	390	395	131	180	106	384	188	177	287	133	1573	1269	1507	1503	1463	133

(*continued on next page*)

Table 4 (*continued*)

	Mn-oxides											Serpentine	Mg-Ni Kerolite
	PIT207-Mn01	PIT207-Mn02	PIT207-Mn03	PIT207-Mn04	PIT207-Mn05	PIT207-Mn06	PIT207-Mn07	PIT207-Mn08	PIT207-Mn09	Average (n = 9)	Std dev.	PIT207-Sil1	PIT207-Sil2
SiO_2	1.11	3.12	6.11	11.56	12.64	12.38	16.56	12.23	10.09	9.53	5.03	42.44	48.26
TiO_2	b.d.l.	b.d.l.	b.d.l.	b.d.l.	0.01	b.d.l.	b.d.l.	b.d.l.	b.d.l.	b.d.l.		0.01	b.d.l.
Al_2O_3	0.31	0.33	0.43	0.96	0.89	0.91	0.89	0.65	0.56	0.66	0.26	0.02	2.68
Fe_2O_3	8.91	18.26	28.28	14.11	17.38	15.46	17.18	17.66	24.29	17.95	5.60	6.46	15.91
MnO	38.79	26.97	18.94	17.28	18.73	16.81	13.64	19.39	19.60	21.13	7.51	0.13	0.08
MgO	1.64	1.46	1.12	1.54	1.97	1.90	4.01	7.48	4.23	2.82	2.08	37.55	14.29
CaO	0.17	0.20	0.18	0.32	0.35	0.30	0.22	0.15	0.10	0.22	0.08	0.19	0.03
Cr_2O_3	11.67	8.25	5.88	5.88	6.06	5.53	4.58	6.27	6.02	6.68	2.10	b.d.l.	1.23
NiO	19.80	17.72	15.70	22.56	23.34	23.35	19.21	15.93	16.01	19.29	3.19	0.49	10.35
Co_3O_4	7.78	10.83	8.31	7.44	7.34	7.14	5.78	4.46	4.57	7.07	1.97	b.d.l.	0.13
Total	90.18	87.14	84.95	81.65	88.71	83.78	82.07	84.22	85.47	85.35	2.88	87.29	92.96
Trace elements													
Sc	n.d.	n.d.	n.d.	n.d.	n.d.	n.d.	n.d.	n.d.	n.d.			n.d.	n.d.
Ti	n.d.	n.d.	n.d.	n.d.	n.d.	n.d.	n.d.	n.d.	n.d.			n.d.	n.d.
V	168	336	n.d.	56.0	n.d.	n.d.	560	284	211	269	172.3	504	616
Cr	79,849	56,449	40,233	40,233	41,464	37,838	31,338	42,901	41,191	45,722	14,386	n.d.	8416
Mn	300,418	208,875	146,685	133,829	145,059	130,189	105,638	150,170	151,797	163,629	58,182	1007	620
Co	57,122	79,515	61,013	54,626	53,891	52,423	42,438	32,746	33,554	51,925	14,481	n.d.	954
Ni	155,599	139,253	123,379	177,289	183,418	183,497	150,963	125,187	125,815	151,600	25,044	3851	81,336
Cu	n.d.	n.d.	n.d.	n.d.	n.d.	n.d.	n.d.	n.d.	n.d.			n.d.	n.d.
Zn	n.d.	n.d.	n.d.	n.d.	n.d.	n.d.	n.d.	n.d.	n.d.			n.d.	n.d.

1996; Koeppenkastrop and De Carlo, 1992; Ohta and Kawabe, 2001) and subsequent precipitation of Ce^{4+} into highly immobile and insoluble cerianite (CeO_2) and/or rhabdophane (Ce-phosphate; Aiglsperger et al., 2016; Janots et al., 2015). The progressive dissolution of secondary Mn-oxides as the weathering proceeds will contribute to fractionate REE by leaching out all trivalent REE, leaving the most weathered horizons enriched in Ce.

5.2. Sc concentration at the goethite-to-hematite transition

The goethite-hematite transition has been widely investigated in the past years (e.g. Cornell and Schwertmann, 2003; Cudennec and Lecerf, 2006; Gialanella et al., 2010; Goss, 1987; Gualtieri and Venturelli, 1999; Langmuir, 1971; Schwertmann, 1985; Schwertmann and Murad, 1983; Tardy and Nahon, 1985). The thermally induced transformation of goethite to hematite occurs at about 250 °C, this temperature being by far above to those occurring in laterites. (e.g. Gialanella et al., 2010; Gualtieri and Venturelli, 1999). Therefore, the direct formation of hematite from the dehydration of crystalline goethite is unlikely in this environment. Most likely, this transition occurs after goethite dissolution followed by the precipitation of hematite after a ferrihydrite precursor (Goss, 1987; Schwertmann, 1985; Tardy and Nahon, 1985). Near neutral pH (6–8; Gleeson et al., 2003; Marsh et al., 2013), relatively high temperature (up to ~45 °C) and a decrease of water activity at the top of the lateritic profile are much more in favor of hematite formation compared to more acidic pH conditions (4–6; Fandeur et al., 2009b), high water activity and high moisture that favor the precipitation of goethite deeper in the profile (Cornell and Schwertmann, 2003; Schwertmann, 1985; Schwertmann and Murad, 1983; Tardy and Nahon, 1985).

Teitler et al. (2019) suggest that the decrease of bulk Sc concentrations observed from yellow limonite to red limonite and ferricrete is related to the Sc content in goethite itself. However, given that Sc is exclusively controlled by goethite and hematite at the uppermost horizons (Fig. 10) and that Sc contents in goethite is greater than in hematite (Fig. 9; Table 4), the characteristic decrease of bulk Sc concentrations in the uppermost horizons of the regolith may be also controlled by the increasing amount of hematite with respect to goethite. To illustrate this postulate, the Raman spectra of five iron oxides (3 goethites and 2 hematites) from the PIT207C pisolith sample are plotted in relation with their Sc concentrations (Fig. 11a and b). In this example, the samples PIT207C5-8, C9-10 and C14 display intermediate, transitional spectra between the two goethite (PIT207C15) and hematite (PIT207C12-13) end-members (Fig. 11a). This progressive transition is well highlighted by the increasing intensity of the peak at 225 cm^{-1}, which is very low in intensity in goethite and is the third most intense in hematite. Therefore, the 225 cm^{-1} peak can be considered as a good proxy for characterizing the mixture between goethite and hematite. Related to Sc concentrations, Fig. 11b shows that for an increasing intensity I(225), Sc content is decreasing in iron oxides from PIT207C sample. Similar results were obtained on other pisolith samples (Fig. 11c), thus demonstrating that the progressive dissolution of goethite and subsequent crystallization of hematite leads to the mobilization of Sc. Assuming that Sc is adsorbed on goethite as proposed by Chassé et al. (2017) implies that only a small fraction of Sc (± 50%) is retained and integrated in the structure of hematite. However, considering Sc as integrated in the crystal structure of goethite, as postulated by Muñoz et al. (2017), suggests that the capacity of Sc substitution in hematite is lower than in goethite. Although further investigations are needed to discriminate between both hypotheses, the latter would make Sc behavior very similar to that of Al, since it was demonstrated that the natural goethite is able to integrate in its structure twice the amount of Al (up to 33% Al) compared to hematite (< 15% Al; Cornell and Schwertmann, 2003; Schwertmann and Carlson, 1994; Schwertmann et al., 2000; Trolard et al., 1995).

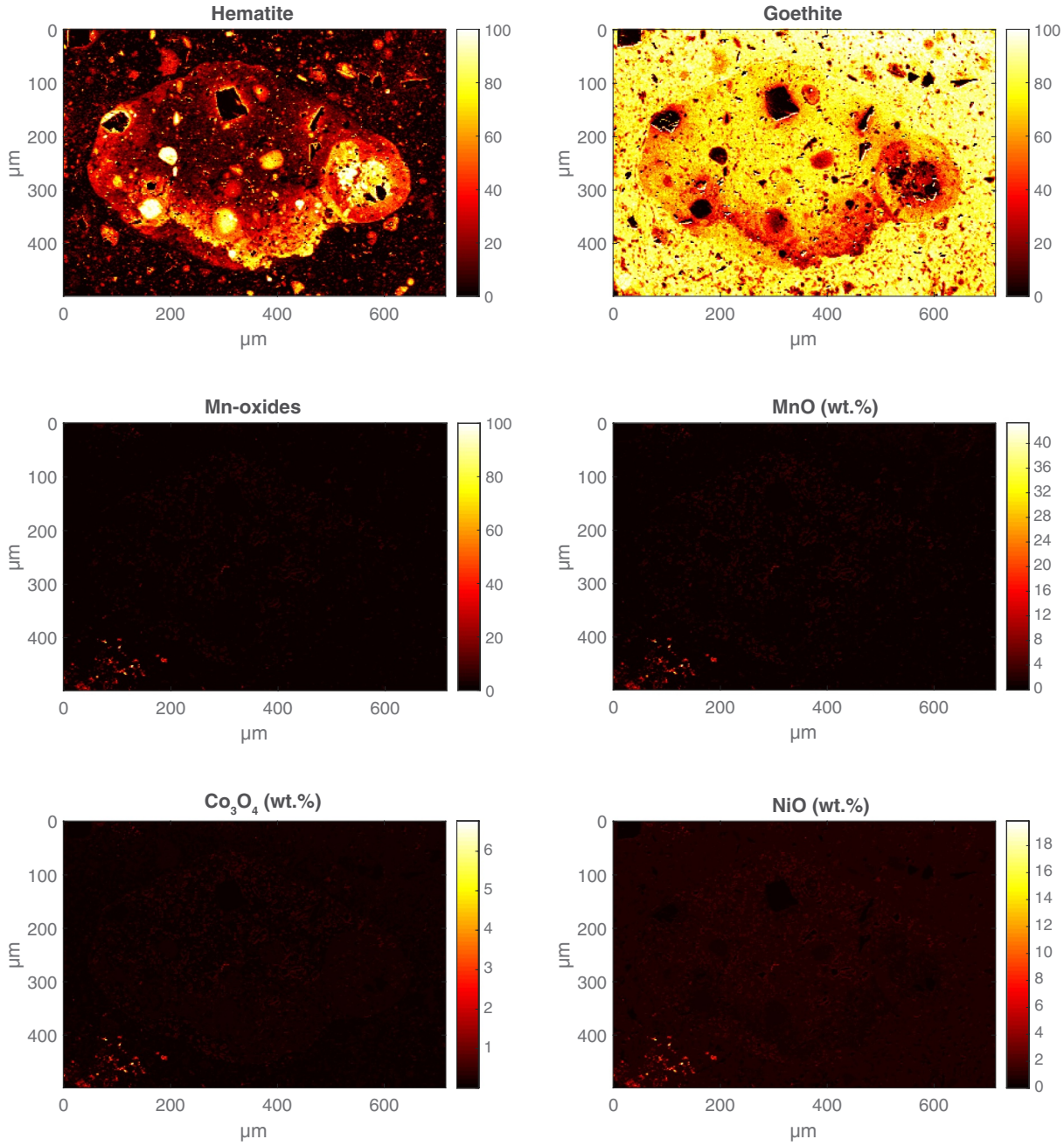

Fig. 9. Mineral phases and chemical maps calculated on the basis of EPMA mapping. Phase maps show the distribution and quantification (in %) for each pixel of goethite, hematite and relicts of Mn-oxides. Chemical maps show the concentrations of MnO, NiO and Co_3O_4 and highlight that highest concentrations of these elements are measured in Mn-oxides.

5.3. Sc in New Caledonia: a new (by-product) resource?

To date the global supply and consumption of scandium is estimated to be about 10 to 15 tons per year, mainly in the use of Al-Sc alloys and solid oxide fuel cells. Sc is almost exclusively recovered as a by-product from residues, tailings and waste liquors in the production of other metals (Gambogi, 2018; Wang et al., 2011), but recent discoveries of unusual high-grade lateritic Sc ores in Eastern Australia (up to 1000 ppm Sc) would make it potentially mined as a primary product (Chassé et al., 2017; Jaireth et al., 2014). In New Caledonia, such concentrations are not observed. With a maximum of > 100 ppm and an average of 80 ppm of Sc, New Caledonia Ni-laterites are much more comparable to those located in Cuba, Dominican Republic or Indonesia (Aiglsperger et al., 2016; Maulana et al., 2016). To these grades, Sc may only be valuable as a by-product of Ni(Co) production. The main limitation regarding Sc exploitation in New Caledonia is that currently most of Ni is recovered from saprolith ore by pyrometallurgical extraction, while Sc is mainly concentrated in overlying laterite ore and is

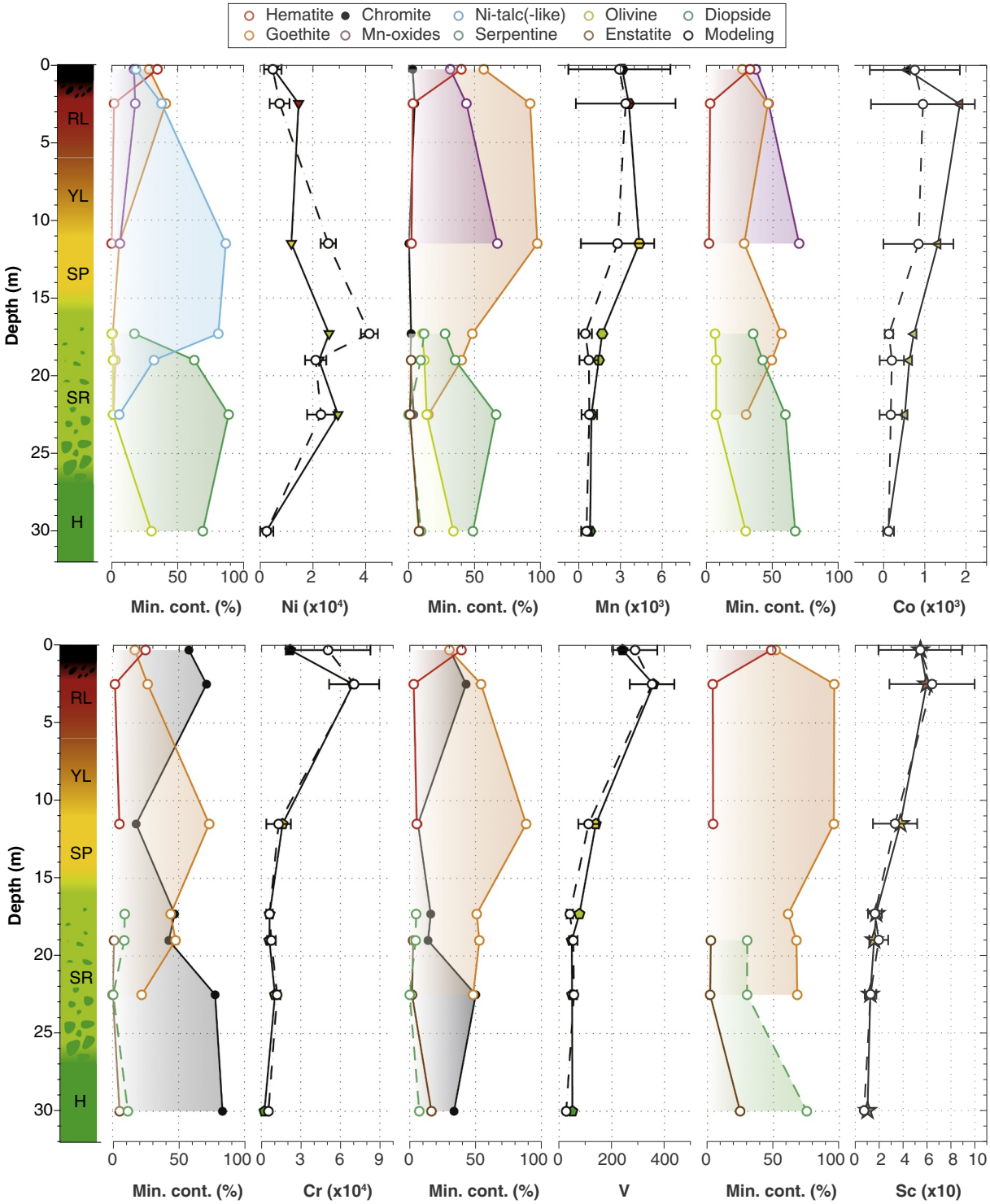

Fig. 10. Calculated element distribution along the CT weathering profile (from mineral concentrations and modal abundance) Error bars are the 2σ standard deviation calculated from the standard deviation on concentrations (Table 4). Min. Con. indicates the mineral contribution (in %) involved in the bulk rock element concentration. Minerals which contribute to < 5% of the bulk element budget are not considered. All element concentrations are in ppm. Point styles are the same as in Fig. 5. H: harzburgite; SR: saprock; SP: saprolite; YL and RL: yellow and red limonites. (For interpretation of the references to colour in this figure legend, the reader is referred to the web version of this article.)

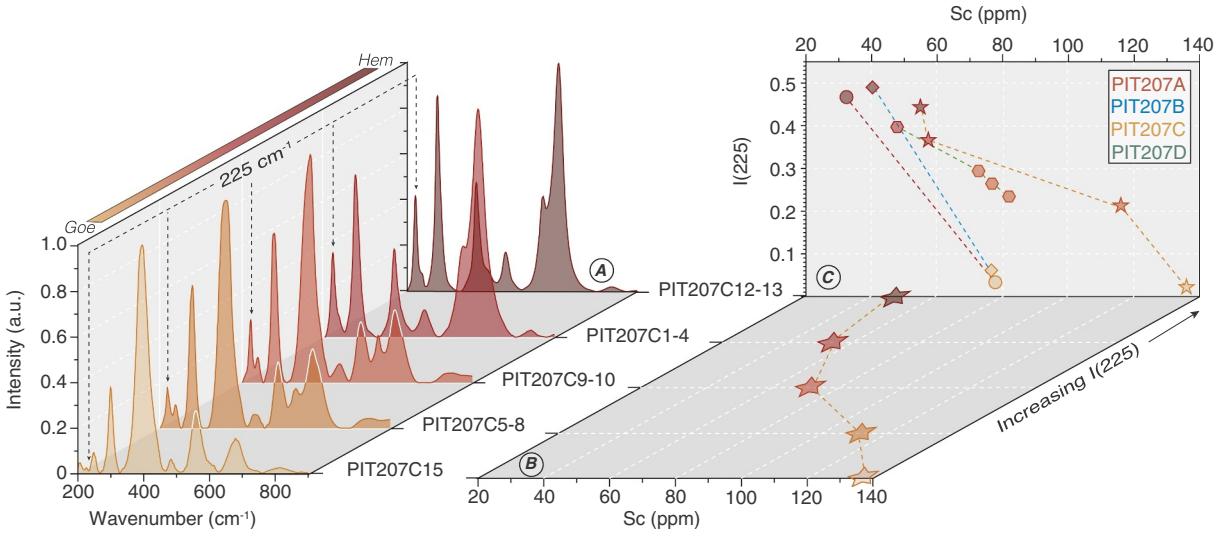

Fig. 11. a) Raman spectra of iron oxides (goethite and hematite) from sample PIT207c, ranked by order of peak intensity at 225 cm^{-1} (I(225)). **b**) Evolution of Sc concentrations with increasing I(225) in iron oxides of PIT207c pisolith. **c**) Same as b) for other pisoliths of sample PIT207 (Fig. 3).

most commonly recovered by using hydrometallurgical processes (Wang et al., 2011). Presently, such processes are exclusively used in the south of the island, i.e. the Goro mine (Vale), for the recovering of Ni and Co from oxide deposits (Flett, 2004; Wells et al., 2009). The potential of Sc production in New Caledonia is thus limited to date. However, considering increasing market interest, low production at the world scale and recent improvements on recovering methods (up to ~85%; SIMN, 2018), it could be worth considering Sc as a future (by-product) resource of Ni-laterites in New Caledonia.

Given the very low REE content of New Caledonia peridotites compared to more conventional REE deposits (Chakhmouradian and Wall, 2012), it is clear that New Caledonia laterites can hardly be considered as a potential source of REE, even as a by-product. In addition, although concentrations in the order of 200 ppm were measured in laterites developed on mafic intrusives, these occurrences are too scarce at the ophiolite scale to be of an economic interest.

6. Conclusions

By using complementary mineralogical and geochemical data, this study shows that some critical and transition metals may be significantly enriched in the different horizons that compose the New Caledonia lateritic profile:

(1) After dissolution of primary mineral, nickel is likely to be integrated into secondary Ni-bearing phyllosilicates in saprolitic horizons. In agreement to that was concluded by previous studies, Ni budget is chiefly controlled by goethite in upper horizons (i.e. laterites and ferricrete), even if Mn-oxides and relicts of silicate can also integrate substantial amount of Ni.
(2) Highest manganese and cobalt concentrations are observed at the transition between saprolite and limonites, where both elements precipitate in Mn-oxides. In limonites, Mn-oxides are not stable due to changing pH-Eh conditions, increasing dryness and bacterial activities. They are readily dissolved and only a small fraction of Mn and Co is integrated to iron oxides. The remaining fraction is solubilized and transferred downwards.
(3) Chromium and vanadium are essentially concentrated in primary chromites, which are highly resistant to weathering. Bulk rock concentrations in each horizon are thus directly dependent on the amount of residual chromite embedded in samples. Cr and V released during the weathering of primary silicates (mainly pyroxenes) are incorporated into iron oxides by adsorption or Fe-substitution. Their concentrations increase with increasing weathering to reach their highest concentrations at the top of the lateritic profile.
(4) Although absolute REE concentrations are very low, our results show that REE are mobilized and enriched during the weathering of peridotite. Highest concentrations are observed at the transition between saprolites and limonites, showing that REE are mainly controlled by Mn-oxides. Only tetravalent Ce remains concentrated in limonites and ferricrete, likely in the form of cerianite (CeO_2). Given the overall very low REE grade, New Caledonia can hardly be considered as a potential valuable source of REE.
(5) Contrarily to REE, scandium enrichment is of about 10 times greater in laterites regarding its initial concentration in parent rocks (8 to 80 ppm Sc in average, > 100 ppm locally at the top of yellow limonite). Sc is mainly released from the dissolution of pyroxenes and integrated in goethite. Our study shows that Sc may be mobilized at the top of the profile, and that this mobilization is likely related to the dissolution of goethite and subsequent crystallization of hematite. As a consequence, released Sc is transferred downward in the profile and accumulates in yellow limonite, where the amount of goethite is the highest. Although Sc concentrations in New Caledonia laterites are far below those of world class Sc deposits recently found in Australia, Sc could become an interesting potential (by-product) resource of Ni-laterites in New Caledonia in the next few decades.

Acknowledgements

This work has been funded and logistically supported by the French National Research Agency through the national program “Investissements d'avenir” of the Labex Ressources 21 with the reference ANR-10-LABX-21-

RESSOURCES21 and by the National Centre for Technological Research CNRT "Nickel et son environnement" based in Nouméa, New Caledonia (Project grant: 8PS2013-CNRT.CNRS/SCANDIUM). The authors kindly thank Marie-Camille Caumon, Olivier Rouer and Chantal Peiffert respectively for their help during Raman spectroscopy, EPMA and LA-ICP-MS data acquisitions. Clément Marcaillou (ERAMET-SLN), Clément Couteau and Maxime Drouillet (Koniambo SAS) and Willy Foucher (SMT-MKN) are acknowledged for their technical supports during field campaigns. Mathieu Chassé and Robert A. Ayuso are kindly acknowledged for their very helpful comments that helped to significantly improve the paper.

Appendix A. Development of a new iron oxide standard: StdGoe 1.1

In literature, previous studies performing in situ trace element quantification on iron oxides used ^{57}Fe as internal standard and the silicate standard glass NIST SRM 610 for signal calibration (e.g. Aiglsperger et al., 2016; Green and Watling, 2007; Huelin et al., 2006). Same parameters were applied in this study during first in situ measurements of iron oxides. For elements measured by both EMPA and LA-ICP-MS, concentrations measured by the latter were systematically greater (up to 300%, typically 20–50%; Fig. A1). Two main reasons may explain these discrepancies: (i) the difference of spot size between EMPA (~1 μm) and LA-ICP-MS (44 to 90 μm), and/or (ii) the difference of matrix between iron oxides and the silicate standard NIST SRM 610 used for signal calibration. The difference of spot size is unlikely to explain these overestimations since no similar discrepancies were observed during the measurements of silicate minerals. On the contrary the significant difference in Fe content between NIST SRM 610 standard (458 ± 9 ppm Fe; Jochum et al., 2011) and iron oxides (up to 92 wt% Fe_2O_3) may account for such misfit between EMPA and LA-ICP-MS data. Therefore, a new in-house iron oxide standard was developed to ensure a better accuracy of LA-ICP-MS measurements.

A.1. Preparation procedure

About four kilograms of pisoliths sampled in various parts of the Koniambo massif were chosen as starting material. Pisoliths were first crushed in a disc crusher to obtain a 250 μm grain sized powder. Chromite grains were then separated from other iron oxides using a Frantz isodynamic magnetic separator. The powder was then subjected to several steps of crushing, sieving and gravity separation in a distilled water column to ensure the recovering of powder of a grain size < 10 μm for a particule specific gravity of 4.27 $g{\cdot}cm^{-3}$, corresponding to the gravity of goethite. The upper threshold of 10 μm was chosen for the particule size to ensure the homogeneity of the standard and optimize the reproducibility of LA-ICP-MS measurements even at small spot size (down to 44 μm, see Sections 2 and 3 below). The chemical composition of the powder was then determined at SARM by ten independent analyses, and ~500 mg was pressed to form a 2 mm thick pellet for LA-ICP-MS measurements.

A.2. Mineralogy of the StdGoe 1.1 standard

The standard homogeneity in term of mineralogy was tested by Raman spectroscopy (Fig. A2). About 50 spectra were acquired randomly on the pellet surface and confirm that the standard mainly consists of goethite, with typical peaks at 247, 299, 393, 483 and 559 cm^{-1}. Nevertheless, small peaks at 225, 293, 612 and 668 cm^{-1}, corresponding to peaks with the highest standard deviation, may indicate the presence of minute nanograins of hematite or, alternatively, grains with a transitional structure between goethite and hematite.

A.3. Chemical homogeneity and reproducibility of StdGoe 1.1 measurements by LA-ICP-MS at 44 and 90 μm spot size

The reproducibility of standard measurements by LA-ICP-MS was checked by performing 60 analyses at spot sizes of 44 and 90 μm, randomly on

Table A1
Comparison between average number of counts and concentrations based on 60 measurements using two spot sizes of 90 μm and 44 μm (30 measurements each). The conversion from count to concentration is calculated using Fe as internal standard.

Elements	ICP-MS	LA-ICP-MS 90 μm (n = 30)				LA-ICP-MS 44 μm (n = 30)			
	StdGoe1.1	Counts	RSD (%)	[C] ppm	RSD (%)	Counts	RSD (%)	[C] ppm	RSD (%)
Mg	1025	35,549	9.6	1020	8.14	6109	9.84	1028	9.19
Al	31,595	648,258	12.6	31,619	2.31	183,924	7.6	31,860	2.3
Si	7806	82,223	9.78	7713	6.6	21,073	15.6	7690	13.3
Sc	54.7	10,483	12.9	54.5	3.1	3091	8.33	55	3.73
Ti	1019	1497	13.7	1022	3.57	439	10.2	1015	8.2
V	234	8206	20.3	242	6.56	1737	7.61	234	2.94
Cr	17,721	136,961	12	17,470	3.6	39,633	9.09	18,539	5.05
Mn	1.51	1,083,970	12.5	1.54	4.65	311,409	7.83	1.48	3.73
Fe	*530,041*	474,863	12.2	*530,041*	–	138,378	5.44	*530,041*	–
Co	638	55,572	12.4	642	4.23	12,326	14	660	10
Ni	4397	80,267	12.7	4253	2.34	20,561	14.3	4144	10.4
Cu	46.9	780	12.9	45.7	3.13	226	9.89	47.4	4.45
Zn	187	916	9.87	193	2.62	262	11.1	194	6.44

the pellet surface. Table A1 shows the average counts and the relative standard deviation (RSD) for each element at each spot size. These results are converted into concentrations (using ^{57}Fe as internal standard) and compared to the concentration measured by ICP-MS (Fig. A3). RSD obtained on the signal (in counts) is < 13% for most elements with a spot size of 90 µm and < 10% with a spot size of 44 µm. Very similar RSD were obtained during NIST SRM 610 measurements, demonstrating the good homogeneity of the StdGoe 1.1 standard. This assumption is confirmed when the signal is converted to concentrations: the deviations between LA-ICP-MS and ICP-MS results are low, typically < 5% for all elements. The very good reproducibility is shown by RSD values which are usually < 5% at 90 µm and below 10% at 44 µm.

A.4. Application of the new StdGoe 1.1 standard during in situ analyses of iron oxides

Fig. A1 shows the result of a single analyse of a hematite grain (PIT207 A 1-4) calibrated against the NIST SRM 610 on one hand and our newly developed in-house StdGoe 1.1 standard on the other hand. In this example, concentrations determined by LA-ICP-MS and calibrated using the NIST SRM 610 is ~50% greater than those measured by EMPA for most elements, including transition metals. This misfit is clearly corrected by using the goethite standard for calibration. Concentrations measured by LA-ICP-MS fit well with those determined by EMPA. This demonstrates that the analyses of iron oxides are significantly improved using the StdGoe 1.1 for signal calibration. A consequence is that $[Sc]_{StdGoe\ 1.1}$ is systematically lower than $[Sc]_{NIST\ 610}$ of ~20 to 50% and that this discrepancy is also observed for most transition metals. Therefore, previous concentrations measured by LA-ICP-MS in iron oxides and available to date in the literature must be considered with care.

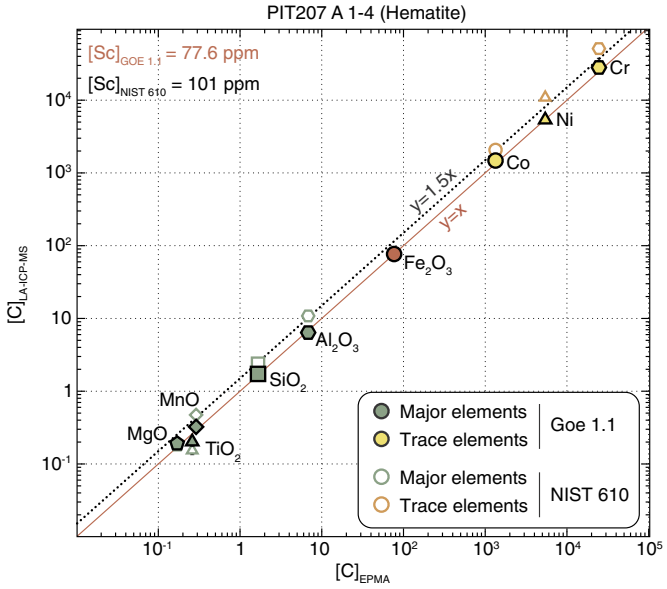

Fig. A1. Comparison between concentrations determined by EPMA and those measured LA-ICP-MS and calibrated against NIST SRM 610 standard (empty symbols) or against our new goethite standard Std Goe 1.1 (filled symbols).

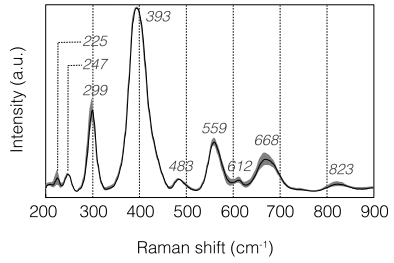

Fig. A2. Average of 50 Raman spectra measured on the pellet surface of StdGoe 1.1 standard showing that the standard is almost exclusively compose by goethite. However the presence of minute grains of hematite cannot be excluded since peaks where the standard deviation is the highest (i.e. at 225, 293, 612 and 668 cm^{-1}) are typical of hematite. This may also reflect the presence of goethite with intermediate Raman signature between that of goethite and that of hematite, similarly to that was described in Figs. 5 and 11. The 2σ standard deviation is indicated by the grey area.

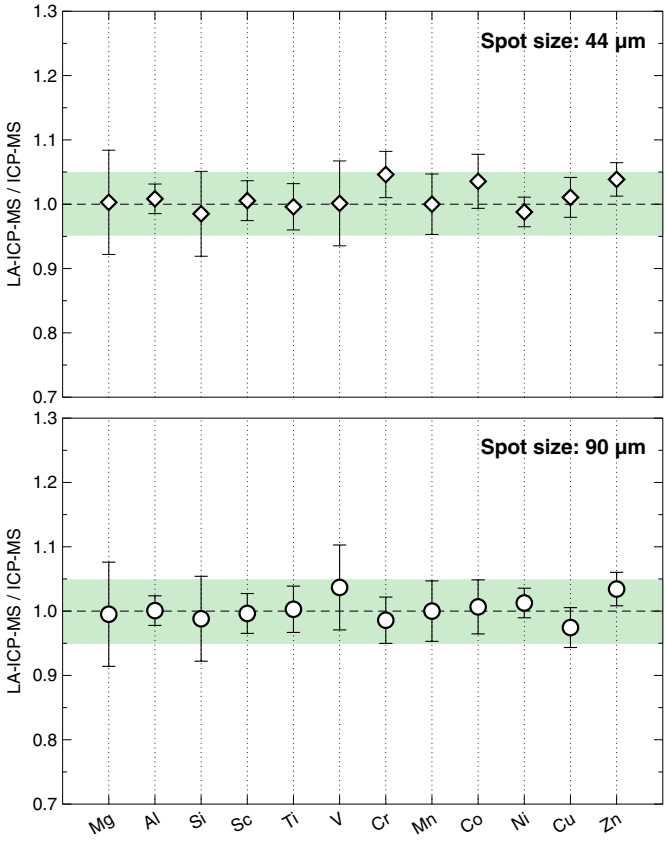

Fig. A3. Comparison between concentrations measured by ICP-MS and LA-ICP-MS on StdGoe 1.1 standard for Mg, Al, Si, and all transition metals. Error bars correspond to the relative standard deviation calculated on the basis of 30 different analyzes by LA-ICP-MS at each spot size. The green area corresponds to a relative deviation of 5%.

Appendix B. Supplementary data

Supplementary data to this article can be found online at https://doi.org/10.1016/j.gexplo.2018.11.017.

References

Aiglsperger, T., Proenza, J.A., Lewis, J.F., Labrador, M., Svojtka, M., Rojas-Purón, A., Longo, F., Ďurišová, J., 2016. Critical metals (REE, Sc, PGE) in Ni laterites from Cuba and the Dominican Republic. Ore Geol. Rev. 73, 127–147.

Allègre, C.J., Prinzhofer, A., 1985. Residual peridotites and the mechanisms of partial melting. Earth Planet. Sci. Lett. 74, 251–265.

Anders, E., Grevesse, N., 1989. Abundances of the elements - Meteoritic and solar. Geochim. Cosmochim. Acta 53, 197–214.

Audet, M.-A., 2009. Le massif du Koniambo, Nouvelle-Calédonie Formation et obduction d'un complexe ophiolitique du type SSZ. Enrichissement en nickel, cobalt et scandium dans les profils résiduels. Université de la Nouvelle-Calédonie et Université du Quebec, pp. 355.

Bau, M., Koschinsky, A., Dulski, P., Hein, J.R., 1996. Comparison of the partitioning behaviours of yttrium, rare earth elements, and titanium between hydrogenetic marine ferromanganese crusts and seawater. Geochim. Cosmochim. Acta 60, 1709–1725.

Beukes, J., Giesekke, E., Elliott, W., 2000. Nickel retention by goethite and hematite. Miner. Eng. 13, 1573–1579.

Braun, J., Pagel, M., Muller, J., Bilong, P., Michard, A., Guillet, B., 1990. Cerium anomalies in lateritic profiles. Geochim. Cosmochim. Acta 54, 781–795.

Butt, C.R.M., Cluzel, D., 2013. Nickel laterite ore deposits: weathered serpentinites. Elements 9, 123–128.

Carignan, J., Hild, P., Mevelle, G., Morel, J., Yeghicheyan, D., 2001. Routine analyses of trace elements in geological samples using flow injection and low pressure on-line liquid chromatography coupled to ICP-MS: a study of geochemical reference materials BR, DR-N, UB-N, AN-G and GH. Geostand. Geoanal. Res. 25, 187–198.

Castor, S.B., Hendrick, J.B., 2006. Rare earth elements. In: Industrial Minerals and Rocks. SME. fieldexexploration.com (pp. 769–792).

Cathelineau, M., Caumon, M.-C., Massei, F., Brie, D., Harlaux, M., 2015a. Raman spectra of Ni-Mg kerolite: effect of Ni-Mg substitution on O-H stretching vibrations. J. Raman Spectrosc. 46, 933–940.

Cathelineau, M., Quesnel, B., Gautier, P., Boulvais, P., Couteau, C., Drouillet, M., 2015b. Nickel dispersion and enrichment at the bottom of the regolith: formation of pimelite target-like ores in rock block joints (Koniambo Ni deposit, New Caledonia). Mineral. Deposita 51, 271–282.

Cathelineau, M., Myagkiy, A., Quesnel, B., Boiron, M.-C., Gautier, P., Boulvais, P., Ulrich, M., Truche, L., Golfier, F., Drouillet, M., 2016. Multistage crack seal vein and hydrothermal Ni enrichment in serpentinized ultramafic rocks (Koniambo massif, New Caledonia). Mineral. Deposita 1–16.

Chakhmouradian, A.R., Wall, F., 2012. Rare earth elements: minerals, mines, magnets (and more). Elements 8, 333–340.

Chassé, M., Griffin, W.L., O'Reilly, S.Y., Calas, G., 2017. Scandium speciation in a world-class lateritic deposit. Geochemical Perspectives Letters 105–114.

Cluzel, D., Meffre, S., 2002. L'unité de la Boghen (Nouvelle-Calédonie, Pacifique sud-ouest): un complexe d'accrétion jurassique. Données radiochronologiques préliminaires U-Pb sur les zircons détritiques. C. R. Geosci. 334, 867–874.

Cluzel, D., Aitchison, J., Picard, C., 2001. Tectonic accretion and underplating of mafic terranes in the late Eocene intraoceanic fore-arc of New Caledonia (Southwest Pacific): geodynamic implications. Tectonophysics 340, 23–59.

Cluzel, D., Maurizot, P., Collot, J., 2012. An outline of the Geology of New Caledonia; from Permian-Mesozoic Southeast Gondwanaland active margin to Cenozoic obduction and supergene evolution. Episodes 35, 72–86.

Commission, E, 2011. Critical Raw Materials for the EU-Report of the Ad-hoc Working Group on Defining Critical Raw Materials. (Report of the Ad hoc Working Group on defining critical raw materials).

Commission, E, 2014. Report on critical raw materials for the EU. In: Report of the Ad hoc Working Group on Defining Critical Raw Materials. 41.

Commission, E, 2017. Study on the review of the list of critical raw materials. In: Report of the Ad hoc Working Group on Defining Critical Raw Materials. 93.

Cornell, R.M., Schwertmann, U., 2003. The Iron Oxides: Structure, Properties, Reactions, Occurences and Uses. Wiley-VCH.

Cudennec, Y., Lecerf, A., 2006. The transformation of ferrihydrite into goethite or hematite, revisited. J. Solid State Chem. 179, 716–722.

Dequincey, O., Chabaux, F., Clauer, N., Sigmarsson, O., Liewig, N., Leprun, J.C., 2002. Chemical mobilizations in laterites: evidence from trace elements and 238U-234U-

230Th disequilibria. Geochim. Cosmochim. Acta 66, 1197–1210.
Dequincey, O., Chabaux, F., Leprun, J., Paquet, H., Clauer, N., Larque, P., 2006. Lanthanide and trace element mobilization in a lateritic toposequence: inferences from the Kaya laterite in Burkina Faso. Eur. J. Soil Sci. 57, 816–830.
Doebelin, N., Kleeberg, R., 2015. Profex: a graphical user interface for the Rietveld refinement program BGMN. J. Appl. Crystallogr. 48, 1573–1580.
Dublet, G., Juillot, F., Morin, G., Fritsch, E., Fandeur, D., Ona-Nguema, G., Brown Jr., G.E., 2012. Ni speciation in a New Caledonian lateritic regolith: a quantitative X-ray absorption spectroscopy investigation. Geochim. Cosmochim. Acta 95, 1–40.
Dublet, G., Juillot, F., Morin, G., Fritsch, E., Fandeur, D., Brown, G.E., 2015. Goethite aging explains Ni depletion in upper units of ultramafic lateritic ores from New Caledonia. Geochim. Cosmochim. Acta 160, 1–15.
Eliopoulos, D., Economou-Eliopoulos, M., 2000. Geochemical and mineralogical characteristics of Fe-Ni- and bauxitic-laterite deposits of Greece. Ore Geol. Rev. 16, 41–58.
Emsley, J., 2014. Unsporting scandium. Nat. Chem. 6, 1025.
Fandeur, D., Juillot, F., Morin, G., Olivi, L., Cognigni, A., Ambrosi, J.-P., Guyot, F.o., Fritsch, E., 2009a. Synchrotron-based speciation of chromium in an Oxisol from New Caledonia: Importance of secondary Fe-oxyhydroxides. Am. Mineral. 94, 710.
Fandeur, D., Juillot, F., Morin, G., Olivi, L., Cognigni, A., Webb, S.M., Ambrosi, J.-P., Fritsch, E., Guyot, F.o., Brown Jr., G.E., 2009b. XANES evidence for oxidation of Cr (III) to Cr(VI) by Mn-Oxides in a Lateritic Regolith developed on Serpentinized Ultramafic Rocks of New Caledonia. Environ. Sci. Technol. 43, 7384–7390.
de Faria, D.L.A., Venâncio Silva, S., de Oliveira, M.T., 1997. Raman microspectroscopy of some iron oxides and oxyhydroxides. J. Raman Spectrosc. 28, 873–878.
Flett, D.S., 2004. Cobalt-nickel separation in hydrometallurgy: a review. Chem. Sustain. Dev. 12, 81–91.
Fritsch, E., Juillot, F., Dublet, G., Fonteneau, L., Fandeur, D., Martin, E., Caner, L., Auzende, A.L., Grauby, O., Beaufort, D., 2016. An alternative model for the formation of hydrous Mg/Ni layer silicates ('deweylite'/'garnierite') in faulted peridotites of New Caledonia: I. Texture and mineralogy of a paragenetic succession of silicate infillings. Eur. J. Mineral. 28, 295–311.
Gambogi, J., 2018. Scandium, U.S. Geological Survey, Mineral Commodity Summaries. pp. 144–145.
Gerth, J., 1990. Unit-cell dimensions of pure and trace metal-associated goethites. Geochim. Cosmochim. Acta 54, 363–371.
Gialanella, S., Girardi, F., Ischia, G., Lonardelli, I., Mattarelli, M., Montagna, M., 2010. On the goethite to hematite phase transformation. J. Therm. Anal. Calorim. 102, 867–873.
Gleeson, S.A., Butt, C.R.M., Elias, M., 2003. Nickel laterites: a review. In: Society of Economic Geologists Newsletter. 54. pp. 9–16.
Goss, C.J., 1987. The kinetics and reaction mechanism of the goethite to hematite transformation. Mineral. Mag. 51, 437–451.
Green, R.L., Watling, R.J., 2007. Trace element fingerprinting of Australian ocher using Laser Ablation Inductively Coupled Plasma-Mass Spectrometry (LA-ICP-MS) for the provenance establishment and authentication of indigenous art. J. Forensic Sci. 52, 851–859.
Gualtieri, A.F., Venturelli, P., 1999. In situ study of the goethite-hematite phase transformation by real time synchrotron powder diffraction. Am. Mineral. 84, 895–904.
Guillong, M., Meier, D.L., Allan, M.M., Heinrich, C.A., Yardley, B.W., 2008. Appendix A6: SILLS: a MatLab-based program for the reduction of Laser Ablation ICP-MS data of homogeneous materials and inclusions. In: Mineralogical Association of Canada Short Course. 40. pp. 328–333.
Huelin, S.R., Longerich, H.P., Wilton, D.H.C., Fryer, B.J., 2006. The determination of trace elements in Fe–Mn oxide coatings on pebbles using LA-ICP-MS. J. Geochem. Explor. 91, 110–124.
Jaireth, S., Hoatson, D.M., Miezitis, Y., 2014. Geological setting and resources of the major rare-earth-element deposits in Australia. Ore Geol. Rev. 62, 72–128.
Janots, E., Bernier, F., Brunet, F., Muñoz, M., Trcera, N., Berger, A., Lanson, M., 2015. Ce (III) and Ce(IV) (re)distribution and fractionation in a laterite profile from Madagascar: Insights from in situ XANES spectroscopy at the Ce LIII-edge. Geochim. Cosmochim. Acta 153, 134–148.
Jochum, K.P., Weis, U., Stoll, B., Kuzmin, D., Yang, Q., Raczek, I., Jacob, D.E., Stracke, A., Birbaum, K., Frick, D.A., Günther, D., Enzweiler, J., 2011. Determination of reference values for NIST SRM 610–617 glasses following ISO guidelines. Geostand. Geoanal. Res. 35, 397–429.
Koeppenkastrop, D., De Carlo, E.H., 1992. Sorption of rare-earth elements from seawater onto synthetic mineral particles: an experimental approach. Chem. Geol. 95, 251–263.
Langmuir, D., 1971. Particle size effect on the reaction goethite = hematite + water. Am. J. Sci. 271, 147–156.
Llorca, S., Monchoux, P., 1991. Supergene cobalt minerals from New Caledonia. Can. Mineral. 29, 149–161.
Longerich, H.P., Jackson, S.E., Günther, D., 1996. Laser ablation inductively coupled plasma mass spectrometric transient signal data acquisition and analyte concentration calculation. J. Anal. At. Spectrom. 11, 899–904.
Manceau, A., Calas, G., 1985. Heterogeneous distribution of nickel in hydrous silicates from New Caledonia ore-deposits. Am. Mineral. 70, 549–558.
Manceau, A., Llorca, S., Calas, G., 1987. Crystal chemistry of cobalt and nickel in lithiophorite and asbolane from New Caledonia. Geochim. Cosmochim. Acta 51, 105–113.
Manceau, A., Gorshkov, A.I., Drits, V.A., 1992. Structural chemistry of Mn, Fe, Co, and Ni in manganese hydrous oxides: Part II. Information from EXAFS spectroscopy and electron and X-ray diffraction. Am. Mineral. 77, 1144.
Marchesi, C., Garrido, C.J., Godard, M., Belley, F., Ferré, E., 2009. Migration and accumulation of ultra-depleted subduction-related melts in the Massif du Sud ophiolite (New Caledonia). Chem. Geol. 266, 180–195.
Marker, A., Friedrich, G., Carvalho, A., Melfi, A., 1991. Control of the distribution of Mn, Co, Zn, Zr, Ti and REEs during the evolution of lateritic covers above ultramafic complexes. J. Geochem. Explor. 40, 361–383.
Marsh, J., 1991. REE fractionation and Ce anomalies in weathered Karoo dolerite. Chem. Geol. 90, 189–194.
Marsh, E., Anderson, E., Gray, F., 2013. Nickel-Cobalt laterites—a deposit model. In: U.S. Geological Survey Scientific Investigations Report, pp. 38.
Maulana, A., Sanematsu, K., Sakakibara, M., 2016. An Overview on the Possibility of Scandium and REE Occurrence in Sulawesi, Indonesia. 3. pp. 139–147 (None).
McRae, M.E., 2018. Nickel, U.S. Geological Survey, Mineral Commodity Summaries. pp. 112–113.
Muñoz, M., Pascarelli, S., Aquilantib, G., Naryginac, O., Kurnosovc, A., Dubrovinskyc, L., 2008. Hyperspectral μ-XANES mapping in the diamond-anvil cell: analytical procedure applied to the decomposition of (Mg, Fe)-ringwoodite at the upper/lower mantle boundary. High Pressure Res. 28, 665–673.
Muñoz, M., Ulrich, M., Levard, C., Rose, J., Ambrosi, J.-P., Cathelineau, M., Teitler, Y., Marcaillou, C., Hesse, B., 2017. Distribution and speciation of Sc in lateritic profiles of New Caledonia using synchrotron-XRF and Sc K-edge XANES spectroscopy. In: First International Workshop on the Geochemical Cycle of Nickel, Nancy.
Muñoz, M., Ulrich, M., Cathelineau, M., Mathon, O., 2019. Weathering processes and crystal chemistry of Ni-bearing minerals in saprolite horizon of New Caledonia ophiolite. J. Geochem. Explor (submitted for publication).
Nahon, D., Parc, S., 1990. Lateritic concentrations of manganese oxyhydroxides and oxides. Geol. Rundsch. 79, 319–326.
Ohta, A., Kawabe, I., 2001. REE(III) adsorption onto Mn dioxide (δ-MnO2) and Fe oxyhydroxide: Ce(III) Oxidation by δ-MnO2. Geochim. Cosmochim. Acta 65, 695–703.
Oze, C., Fendorf, S., Bird, D., Coleman, R., 2004. Chromium geochemistry in serpentinized ultramafic rocks and serpentine soils from the Franciscan complex of California. Am. J. Sci. 304, 67–101.
Pirard, C., Hermann, J., O'Neill, H.S.C., 2013. Petrology and geochemistry of the crust-mantle boundary in a Nascent Arc, Massif du Sud Ophiolite, New Caledonia, SW Pacific. J. Petrol. 54, 1759–1792.
Polyak, D.E., 2018. Vanadium, U.S. Geological Survey, Mineral Commodity Summaries. pp. 180–181.
Pourret, O., Davranche, M., 2013. Rare earth element sorption onto hydrous manganese oxide: a modeling study. J. Colloid Interface Sci. 395, 18–23.
Prinzhofer, A., Nicolas, A., Cassard, D., Moutte, J., Leblanc, M., Paris, J., Rabinowitcz, M., 1980. Structures in the New Caledonia peridotites-gabbros: Implications for oceanic mantle and crust. Tectonophysics 69, 85–112.
Quantin, C., Becquer, T., Berthelin, J., 2002. Mn-oxide: a major source of easily mobilisable Co and Ni under reducing conditions in New Caledonia Ferralsols. C. R. Geosci. 334, 273–278.
Scandium International Mining, C, 2018. Scandium International is Rapidly Advancing the World's First Primary Scandium Mine to Production. scandiummining.com.
Schwertmann, U., 1985. The effect of pedogenic environments on iron oxide minerals. Adv. Soil Sci. 171–200 (Springer New York, New York, NY).
Schwertmann, U., Carlson, L., 1994. Aluminum influence on iron oxides: XVII. Unit-cell parameters and aluminum substitution of natural goethites. Soil Sci. Soc. Am. J. 58, 256–261.
Schwertmann, U., Latham, M., 1986. Properties of iron oxides in some new caledonian oxisols. Geoderma 39, 105–123.
Schwertmann, U., Murad, E., 1983. Effect of pH on the formation of goethite and hematite from ferrihydrite. Clay Clay Miner. 31, 277–284.
Schwertmann, U., Pfab, G., 1996. Structural vanadium and chromium in lateritic iron oxides: genetic implications. Geochim. Cosmochim. Acta 60, 4279–4283.
Schwertmann, U., Friedl, J., Stanjek, H., Schulze, D.G., 2000. The effect of Al on Fe oxides. XIX. Formation of Al-substituted hematite from ferrihydrite at 25 °C and pH 4 to 7. Clay Clay Miner. 48, 159–172.
Secchiari, A., Montanini, A., Bosch, D., Macera, P., Cluzel, D., 2016. Melt extraction and enrichment processes in the New Caledonia lherzolites: evidence from geochemical and Sr-Nd isotope data. Lithos 260, 28–43.
Sevin, B., Ricordel Prognon, C., Quesnel, F., Cluzel, D., Lesimple, S., Maurizot, P., 2012. First Palaeomagnetic Dating of Ferricrete in New Caledonia: New Insight on the Morphogenesis and Palaeoweathering of 'Grande Terre'. 24. pp. 77–85.
Shedd, K.B., 2018. Cobalt, U.S. Geological Survey, Mineral Commodity Summaries. pp. 50–51.
Singh, B., Sherman, D.M., Gilkes, R.J., Wells, M.A., Mosselmans, J., 2002. Incorporation of Cr, Mn and Ni into goethite (α-FeOOH): mechanism from extended X-ray absorption fine structure spectroscopy. Clay Miner. 37, 639–649.
Tardy, Y., Nahon, D., 1985. Geochemistry of laterites, stability of Al-goethite, Al-hematite, and Fe^{3+} kaolinite in bauxites and ferricretes; an approach to the mechanism of concretion formation. Am. J. Sci. 285, 865–903.
Teitler, Y., Cathelineau, M., Ulrich, M., Ambrosi, J.-P., Munoz, M., Sevin, B., 2019. Petrology and geochemistry of scandium in New Caledonian Ni-Co laterites. J. Geochem. Explor. 196, 131–155.
Traore, D., Beauvais, A., Chabaux, F., Peiffert, C., Parisot, J., Ambrosi, J.-P., Colin, F., 2008. Chemical and physical transfers in an ultramafic rock weathering profile: part 1. Supergene dissolution of Pt-bearing chromite. Am. Mineral. 93, 22.
Trescases, J., 1973. Weathering and geochemical behaviour of the elements of ultramafic rocks in New Caledonia. In: Bureau of Mineral Resources Geology and Geophysics Department of Minerals and Energy Canberra Bulletin. 141. pp. 149–161.
Trescases, J.-J., 1997. The Lateritic Nickel-Ore Deposits. Springer Berlin Heidelberg, Berlin, Heidelberg, pp. 125–138.
Trolard, F., Bourrie, G., Jeanroy, E., Herbillon, A.J., Martin, H., 1995. Trace metals in natural iron oxides from laterites: a study using selective kinetic extraction. Geochim.

Cosmochim. Acta 59, 1285–1297.
Ulrich, M., Picard, C., Guillot, S., Chauvel, C., Cluzel, D., Meffre, S., 2010. Multiple melting stages and refertilization as indicators for ridge to subduction formation: the New Caledonia ophiolite. Lithos 115, 223–236.
Ulrich, M., Bureau, S., Chauvel, C., Picard, C., 2011. Accurate measurement of rare earth elements by ICP-MS after ion-exchange separation: application to ultra-depleted samples. Geostand. Geoanal. Res. 36, 7–20.
Ulrich, M., Muñoz, M., Guillot, S., Cathelineau, M., Picard, C., Quesnel, B., Boulvais, P., Couteau, C., 2014. Dissolution–precipitation processes governing the carbonation and silicification of the serpentinite sole of the New Caledonia ophiolite. Contrib. Mineral. Petrol. 167, 919–952.
Villanova-de-Benavent, C., Proenza, J.A., Galí, S., García-Casco, A., Tauler, E., Lewis, J.F., Longo, F., 2014. Garnierites and garnierites: Textures, mineralogy and geochemistry of garnierites in the Falcondo Ni-laterite deposit, Dominican Republic. Ore Geol. Rev. 58, 91–109.
Wang, W., Pranolo, Y., Cheng, C.Y., 2011. Metallurgical processes for scandium recovery from various resources: a review. Hydrometallurgy 108, 100–108.
Wells, M.A., Ramanaidou, E.R., Verrall, M., Tessarolo, C., 2009. Mineralogy and crystal chemistry of “garnierites” in the Goro lateritic nickel deposit, New Caledonia. Eur. J. Mineral. 21, 467–483.
Whattam, S.A., Malpas, J., Ali, J.R., Smith, I.E.M., 2008. New SW Pacific tectonic model: Cyclical intraoceanic magmatic arc construction and near-coeval emplacement along the Australia-Pacific margin in the Cenozoic. Geochem. Geophys. Geosyst. 9 (n/a–n/a).
Zoppi, A., Lofrumento, C., Castellucci, E.M., Sciau, P., 2007. Al-for-Fe substitution in hematite: the effect of low Al concentrations in the Raman spectrum of Fe2O3. J. Raman Spectrosc. 39, 40–46.